

Improving Potential Energy Surfaces Using Experimental Feshbach Resonance Tomography

Karl P. Horn,^{†,¶} Luis Itza Vazquez-Salazar,^{‡,¶} Christiane P. Koch,[†] and Markus
Meuwly^{*,‡}

[†]*Dahlem Center for Complex Quantum Systems and Fachbereich Physik, Freie Universität
Berlin, Arnimallee 14, D-14195 Berlin, Germany*

[‡]*Department of Chemistry, University of Basel, Klingelbergstrasse 80, CH-4056 Basel,
Switzerland.*

[¶]*These authors contributed equally*

E-mail: m.meuwly@unibas.ch

September 29, 2023

Abstract

The structure and dynamics of a molecular system is governed by its potential energy surface (PES), representing the total energy as a function of the nuclear coordinates. Obtaining accurate potential energy surfaces is limited by the exponential scaling of Hilbert space, restricting quantitative predictions of experimental observables from first principles to small molecules with just a few electrons. Here, we present an explicitly physics-informed approach for improving and assessing the quality of families of PESs by modifying them through linear coordinate transformations based on experimental data. We demonstrate this "morphing" of the PES for the He-H₂⁺ complex for reference surfaces at three different levels of quantum chemistry and using recent comprehensive Feshbach resonance (FR) measurements. In all cases, the positions and intensities of peaks in the collision cross section are improved. We find these observables to be mainly sensitive to the long-range part of the PES.

Teaser

We introduce a systematic approach based on experimental data to validate and improve molecular potential energy surfaces.

1 Introduction

The potential energy surface (PES) representing the total energy of a molecule is a fundamental concept for characterizing the dynamics both in the gas and condensed phase.^{1,2} With high-quality PESs, the computation of experimental observables becomes possible with predictive power at a quantitative level. On the other hand, while all physical observables depend on it, the PES itself cannot be observed. This raises the question of how to obtain the most accurate PES for a given system. From an electronic structure perspective, it is

known that full configuration interaction (FCI) calculations with large basis sets provide the highest quality for the total energies of a molecule. However, the unfavourable scaling of FCI with the number of electrons and basis functions prevents its routine use for constructing full-dimensional PESs for any molecule consisting of more than a few light atoms. Alternatively, one may approach the question from an experimentalist’s perspective and argue that the “most accurate PES” is the one that best describes physical observations. Such an approach has been developed for diatomic molecules: the rotational Rydberg-Klein-Rees (RKR) method solves the “inversion problem” of obtaining the potential energy curve given spectroscopic information.³ Rotational RKR has also been applied to triatomic van der Waals complexes^{4,5} but cannot be extended to molecules of arbitrary size. Indeed, solving the “inverse problem”, i.e., determining the PES given experimental observables and an evolution equation from which these observables are calculated has in general turned out to be very difficult in chemical physics.⁶ This concerns both the choice of observables as well as the actual inversion procedure.

An alternative that is not particularly sensitive to the dimensionality of the problem is “morphing” PESs.^{7,8} This method exploits the topological relationship between a reference and a target PES. Provided that calculations with the reference PES yield *qualitatively* correct observables $\mathcal{O}_{\text{calc}}$ when compared with experimental observations \mathcal{O}_{exp} , the squared difference $\mathcal{L} = |\mathcal{O}_{\text{calc}} - \mathcal{O}_{\text{exp}}|^2$ can be used to reshape the PES through linear or non-linear coordinate transformations (“morphing”).⁷ It capitalizes on the correct overall topology of the reference PES and transmutes it into a new PES by stretching or compressing internal coordinates and the energy scale, akin to machining a piece of rubber. Alternatives for reshaping PESs are machine learning-based methods such as Δ -ML,⁹ transfer learning,^{10,11} or differential trajectory reweighting.¹² Morphing has been applied successfully to problems in spectroscopy,¹³ state-to-state reaction cross sections,¹⁴ and reaction dynamics¹⁵ for systems with up to 6 atoms.¹⁶ A near-quantitative reference PES has, however, so far not been available for direct

comparison. For scattering experiments with He-H₂⁺ such a PES is now available.

The He-H₂⁺ molecular complex is an ideal proxy for the present work owing to the fact that the PES can be calculated rigorously at the highest level of quantum chemistry (FCI). The complex is also interesting in itself, and the current status of experimental and computational spectroscopy and reaction dynamics has recently been reviewed.¹⁷ He-H₂⁺, which is isoelectronic to H₃, is stable in its electronic ground state and features a rich reaction dynamics and spectroscopy. Experimentally, near-dissociative states^{18,19} and the low-resolution spectroscopy were reported for both, He-H₂⁺ and He-D₂⁺.²⁰ Assignments of the vibrational bands were possible by comparing with bound state calculations utilizing a FCI PES.²¹ Only recently, it was possible to estimate the dissociation energy of ~ 1800 cm⁻¹ from spectroscopic measurements.²⁰ This compares with earlier bound state calculations using the FCI PES predicting a value of $D_0 = 1784$ cm⁻¹.²¹ This value was confirmed from a subsequent focal point analysis resulting in $D_0 = 1789(4)$ cm⁻¹ for para-H₂⁺.²² Furthermore, a range of reactive collision experiments was carried out which yielded total and differential cross sections, depending on the vibrational state of the diatomic,¹⁷ but with marked differences between observed and computed results. In particular, computationally predicted sharp reactive scattering resonances have not been found experimentally as of now.¹⁷ Finally, the role of nonadiabatic couplings is of considerable current interest as a means to clarify the role of geometric phase in reaction outcomes and as a source of friction in the formation of the He-H₂⁺ complex in the early universe. This provides additional impetus for a comprehensive characterization of this seemingly “simple” system.

The present work uses experimentally measured Feshbach resonances for He-H₂⁺²³ to morph potential energy surfaces. Feshbach(-Fano) resonances arise if a bound molecular state on a potential energy surface of a closed channel couples to scattering states in an open channel.^{24,25} The recoil translational energy is determined from measurements which are expected

to probe large spatial areas of a PES and the underlying intermolecular interactions.²⁵ The redistribution of energy due to the Feshbach resonances has recently been mapped out comprehensively for He–H₂⁺ and Ne–H₂⁺ with coincidence velocity map imaging of electrons and cations, yielding very favourable agreement between theory and experiment.²³ In these experiments, the ionic molecular complexes are generated at separations of up to 10 a₀ between the rare gas atom and the molecular ion, confirming that the experiment indeed probes a large spatial extent of the PES, including its long-range part.

Here, morphing is applied to initial PESs ranging from essentially exact FCI (apart from non-Born-Oppenheimer and remaining basis set effects) to medium- and lower-level methods, that is, Multi-Reference Configuration Interaction including the Davidson correction (MRCI+Q) and second-order Møller-Plesset perturbation theory (MP2). This allows us to determine the sensitivity of the PES and information content in the experimental observables about local and global features of the PES and to assess the performance of lower-level methods (e.g. MP2) compared with FCI. We found that starting from a PES of sufficiently high quality, the changes introduced by morphing can be related to parts of the PES that are probed by the experiments. At the same time, additional experimental observables, probing primarily the bound region for He interacting with H₂⁺, will be required for morphing at the lower levels of quantum chemical theory.

2 Results

The three PESs considered in the present work, in decreasing order of rigour, were determined at the FCI, MRCI+Q, and MP2 levels of theory, using Jacobi coordinates R (distance between the centre of mass of the H₂⁺ and He), r (distance between the two hydrogen atoms), and θ (the angle between the two vectors \vec{R} and \vec{r}), see Figure 1A. To set the stage, scattering calculations with the FCI PES are considered which give quite satisfactory results when

compared with the experimental data (Figure 2 A and Table 1). The measured kinetic energy distributions feature a series of peaks which reflect the rovibrational quenching associated with the decay of the Feshbach resonances.²³ On average, the positions of the peak maxima are reproduced to within 10.8 cm^{-1} whereas the maximum intensities, I_{max} , of $P(E)$ differ by 20.9 arb. u. (blue squares in Figure 2A).

Next, morphing is applied to all three PESs, including the FCI PES. The FCI PES has been validated with respect to experiment^{18–20,23} and therefore can serve as a suitable proxy for changes required for PESs at the MRCI+Q and MP2 levels of theory. Two morphing strategies were considered (Figure 1B): For Morphing M1, the total energy was decomposed into one-body ($\mathcal{V}_i^{(1)}$), two-body ($\mathcal{V}_i^{(2)}$) and three-body ($\mathcal{V}^{(3)}$) terms ,

$$V(R, r, \theta) = \mathcal{V}_{\text{He}}^{(1)} + \mathcal{V}_{\text{H}}^{(1)} + \mathcal{V}_{\text{H}^+}^{(1)} + \mathcal{V}_{\text{HeH}}^{(2)}(r_{\text{HeH}}) + \mathcal{V}_{\text{HeH}^+}^{(2)}(r_{\text{HeH}^+}) + \mathcal{V}_{\text{H}_2^+}^{(2)}(r_{\text{H}_2^+}) + \mathcal{V}^{(3)}(R, r, \theta), \quad (1)$$

and the morphing transformation was applied only to the three-body contribution $\mathcal{V}^{(3)}(R, r, \theta)$. Approach M1 is motivated by the assumption that all diatomic potentials $\mathcal{V}_i^{(2)}$ are of high quality so that changes are only required in the higher-order correction three-body term. In the second approach, called “M2”, the morphing transformation maps $(R, r) \rightarrow (\alpha R, \beta r)$ and the total energy is multiplied by ε to obtain the morphed energy. In this case, the PES is globally modified, including the two-body contributions.

Morphing M1 applied to the FCI PES leaves most of the peak positions unchanged, see filled vs. open blue symbols in Figure 2D, but improves the peak heights considerably (by 30 %) as demonstrated in Figure 2E and Table 1 (rightmost column). These improvements are accommodated by reshaping the underlying PES as shown in Figure 3A: In the long-range ($R > 3.0 a_0$), the anisotropy of the morphed PES is somewhat decreased due to reshaping the PES around $\theta = 90^\circ$ (T-shaped geometry). On the other hand, the curvature along the

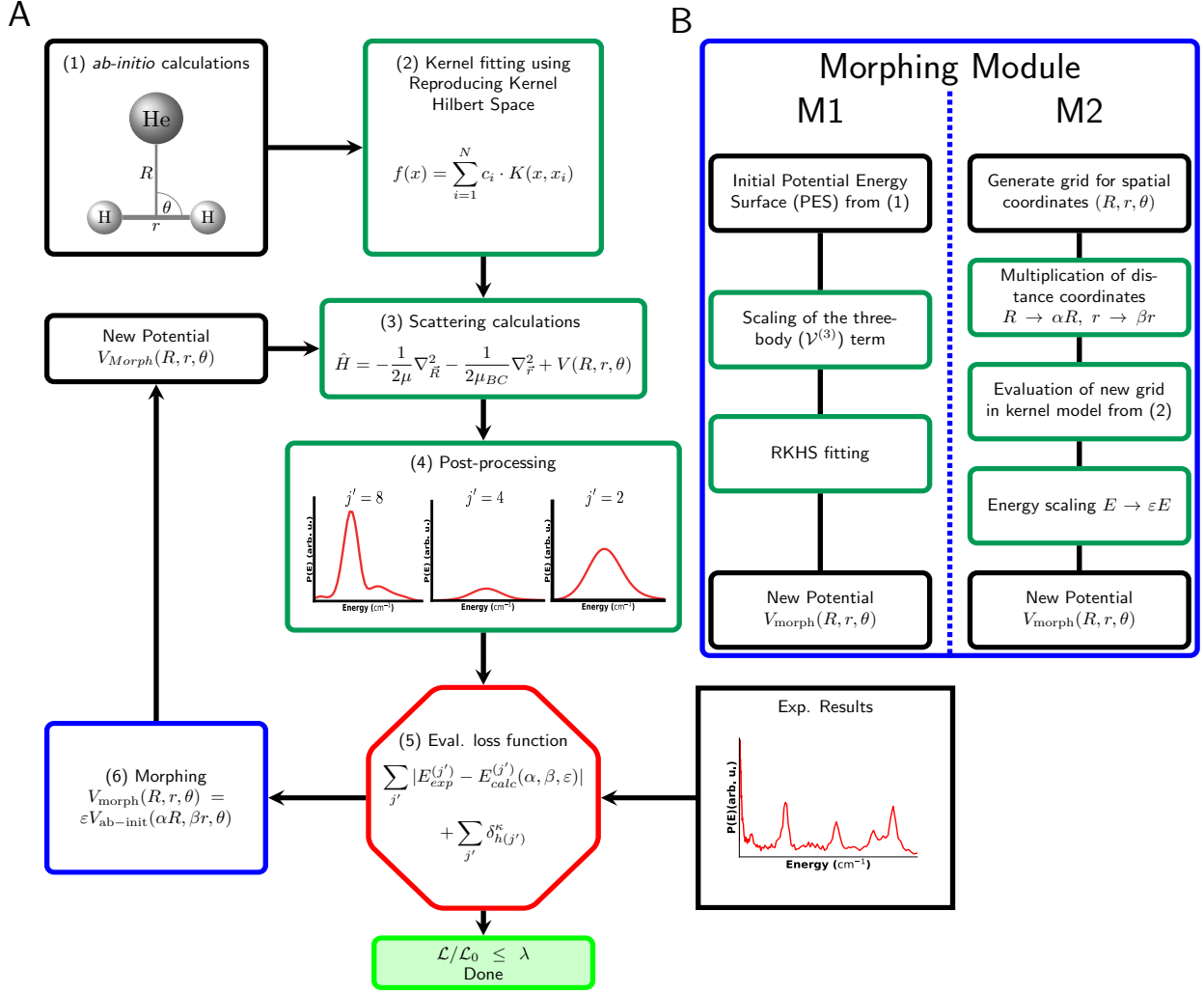


Figure 1: Morphing of *ab initio* potentials based on experimental data. General flowchart of the morphing procedure (A): Module (1) implements the calculation of *ab-initio* points for the system under study, the triatomic HeH_2^+ with the definition of the respective coordinates indicated. Module (2) represents the fitting of the points obtained from the previous step using the Reproducing Kernel Hilbert Space Method, with the functional form used to approximate the given PES. Module (3) corresponds to the scattering calculations performed with the potential obtained in module (2), calculating the eigenstates of the Hamiltonian. Module (4) post-processes the results of the scattering calculations, resulting in the cross sections, with examples for three values of j' displayed. Module (5) evaluates the loss function for morphing, comparing the experimental values of the cross sections with the results of the scattering calculations. Module (6) carries out the actual morphing procedure, as explained in panel B. Morphing results in a new potential, and the procedure continues until the value of the loss function in module (5) does not improve further. The termination conditions are $\mathcal{L}/\mathcal{L}_0 \leq \lambda_{M1} = 0.3$ or $\mathcal{L}/\mathcal{L}_0 \leq \lambda_{M2} = 0.4$ for M1 and M2, respectively where \mathcal{L}_0 is the loss function of the unmorphed cross section, see Figure S6. Panel B: Morphing module (6) for procedures M1 (3-body) and M2 (global).

angular coordinate is increased. One-dimensional cuts along the r_{HH} and R coordinates for a given angle θ show that changes in the PES become more significant at larger values of r_{HH} with small changes in the depth of the potential wells but maintaining the overall shape of the curves (Figures S7 and S8). The changes with respect to R are noticeable for $R < 3.0 a_0$ with small distortions of the energy contours at different angles θ , but maintaining the overall shape of the curves. For larger values of R , the changes are negligible compared with the original PES, reflecting the accurate treatment of the long-range interaction (Figure S7). 2D projections of the combined changes of r_{HH} and R at different angles show that the most pronounced modifications in the shape of the PES concern regions of r_{HH} larger than the equilibrium geometry of H_2^+ , i.e., $r_{\text{HH}} > 2.1 a_0$, and $R = 2 - 3 a_0$ (Figures S9A S10A and S11A).

Table 1: Dissociation energies (D_e in cm^{-1}) for $\text{He}+\text{H}_2^+$, coordinates for the minimum energy structures, R_e and r_e , and root mean squared errors (RMSE) for the peak positions and heights of the kinetic energy spectra for all initial and morphed PESs using both M1 and M2 methods. In all cases, the equilibrium geometry is linear $\text{He}-\text{H}_2^+$, i.e. $\theta = 0$ or $\theta = 180^\circ$.

Surface	D_e (cm^{-1})	R_e/a_0	r_e/a_0	RMSE(E) (cm^{-1})	RMSE(I) (arb. u.)
FCI Initial	2818.9	2.97	2.07	10.8	20.9
FCI Morphed (M1)	2772.0	2.95	2.07	11.9	13.7
FCI Morphed (M2)	2819.1	2.99	2.07	10.8	13.8
MRCI+Q Initial	2557.3	2.98	2.07	10.3	23.9
MRCI+Q Morphed (M1)	3414.7	2.98	2.08	12.2	21.9
MRCI+Q Morphed (M2)	2557.0	3.00	2.03	8.9	17.6
MP2 Initial	2494.0	2.99	2.07	13.1	22.4
MP2 Morphed (M1)	1685.6	2.93	2.12	12.8	10.9
MP2 Morphed (M2)	2492.8	2.97	1.74	10.0	11.8
MP2 Morphed (PES-to-PES)	2502.3	2.98	2.06	13.0(7)	22.9

FCI calculations of entire PESs are only feasible for the smallest chemical systems, i.e. for diatomic or triatomic molecules. For larger systems, quantum chemical methods such as multi-reference configuration interaction or Møller-Plesset perturbation theory need to be

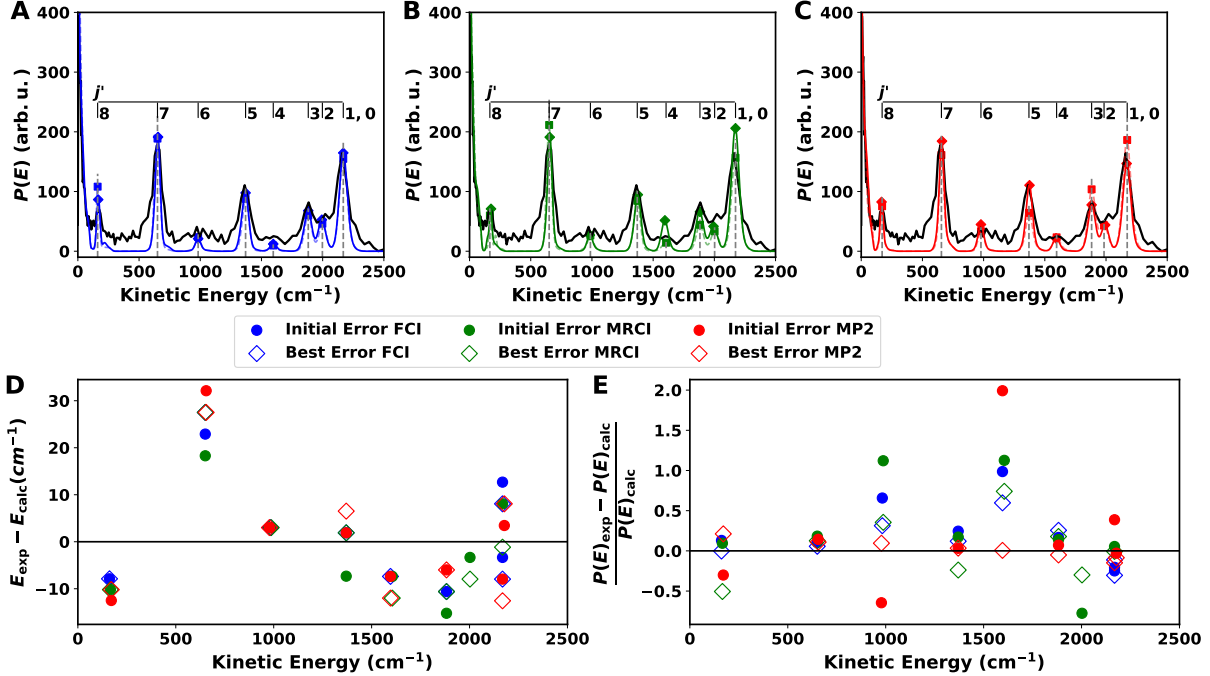


Figure 2: Cross sections obtained from experiment (black, data taken from Ref. 23) and full coupled channels calculations using the unmorphed and M1-morphed PESs for FCI (A), MRCI+Q (B), and MP2 (C). Computed results for the initial (blue, green, red dashed) and best (blue, green, red solid) morphed PESs are reported, with the residuals for the peak positions ($E_{\text{exp}} - E_{\text{calc}}$) and fraction of error in the peak heights ($\frac{P(E)_{\text{exp}} - P(E)_{\text{calc}}}{P(E)_{\text{calc}}}$) for each PES shown in Panels D and E. The statistical measures for all models are summarized in Table 1.

used instead. As reported in the two rightmost columns of Table 1, the initial MRCI+Q and MP2 PESs perform almost on par compared with the initial FCI PES for the positions and intensities of the kinetic energy distributions. On the other hand, the dissociation energy is smaller by more than 10% compared with the FCI PES due to partial neglect of correlation energy in the MRCI+Q and MP2 methods. This confirms that Feshbach resonances are not particularly informative with regards to features of the PES around the minimum energy structure ($R \sim 3.0 a_0$), although the wavefunctions sample this region extensively, see Figure S20. In other words, although an important characteristic of a PES such as the stabilization energy of the complex differs by 10 % or more, the energies and intensities measured in collision experiments are matched within similar bounds.

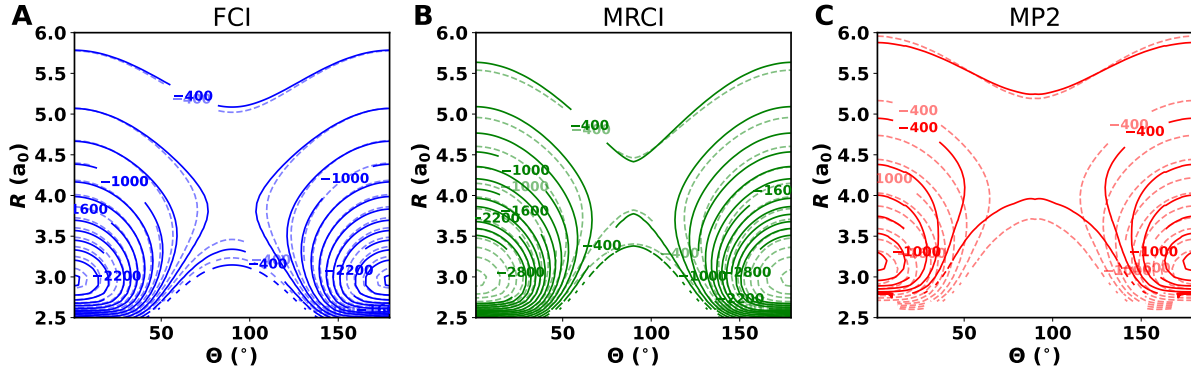


Figure 3: Projections of the PESs for $r_{\text{HH}} = 2.0 a_0$ for the three methods studied here. Isocontours for unmorphed PESs (FCI (blue), MRCI+Q (green) and MP2 (red) from left to right) are shown as dashed lines, whereas the M1-morphed PESs are solid lines. The zero of energy is set by the value at $r = 2.0 a_0$ and $R = \infty$. Energies are in cm^{-1} .

Morphing M1 applied to the MRCI+Q and MP2 PESs supports this observation. The loss function evaluated in module (5) of the optimization, see Figure 1, decreased by 74% and 88% for the two cases, with improvements in the intensities by up to 50% for the MP2 PES, see Table 1 (rightmost column). However, the resulting PESs are clearly unphysical, with pronounced distortions in particular for the MP2 PES, see Figure 3C and dissociation energies either increased by 40 % for MRCI+Q or decreased by 30 % for MP2, respectively. Low-resolution experiments²⁰ provide an estimate for the dissociation energy $D_0 \sim 1800 \text{ cm}^{-1}$, compared with $D_0 = 1794 \text{ cm}^{-1}$ from bound state calculations on the initial FCI PES²¹ which features a well depth of $D_e \sim 2820 \text{ cm}^{-1}$. This value of D_e serves as a reference for the remainder of the present work.

The percentage changes of the parameters $[\alpha, \beta, \varepsilon]$ scaling (R, r, V) provide further information about the transformation induced by morphing the initial PESs. For the FCI PES they are $(-0.6, -3.6, 0.0)\%$ compared with $(-0.6, 11.6, 1.0)\%$ for the MRCI+Q and $(0.3, -9.7, 0.1)\%$ for the MP2 PES. The most significant changes concern the H_2^+ vibrational coordinate r_{HH} for MRCI+Q (+12.0%) and MP2 (-10.0%). Such large changes are problematic since the many-body expansion used for morphing M1, cf. Eq. (1), relies on the

quality of the two-body contributions, i.e., the H_2^+ and HeH^+ potential energy curves. However, MP2 underestimates the experimentally determined dissociation energy of the HeH^+ two-body interaction by 285 cm^{-1} (Figure S12) and accounts for an overall error of $\sim 500 \text{ cm}^{-1}$ in D_e for He-H_2^+ . On the other hand, the two-body term for H_2^+ agrees to within 3 cm^{-1} between the three methods with remaining differences compared with the experiment primarily due to neglect of non-Born-Oppenheimer contributions (Figure S13). To summarize: while M1-morphing improves the match between experimentally measured and calculated observables, it modifies the PES for the lower-level methods in an unphysical way. This is attributed to the fact that M1-morphing operates on the three-body term only and can thus not compensate for inaccuracies in the two-body contributions to the overall PES. In contrast, for FCI the changes for all characteristics of the morphed PES are moderate, underscoring the accuracy of both, the initial and morphed PESs from FCI calculations.

To reduce the dependence of the morphed PESs on the quality of the two-body contributions, morphing M2 was carried out. M2-morphing acts *globally* and independently on each of the internal degrees of freedom, see Figure 1. This makes M2 less prone to overcompensatory effects as observed for M1-morphing. For the MRCI+Q PES the improvement in the observables amounts to $\approx 14 \%$ for the peak positions and $\approx 26 \%$ for the peak heights. At the same time the changes in the PES are moderate, see Figure 4B, and the dissociation energy does not change (Table 1) although the energy scaling parameter, ε was allowed to vary. Similarly, for MP2, the RMSE for the positions and heights of the peaks improve by about 22% and 47% , respectively. Contrary to M1, morphing M2 does not significantly modify the well depth as reflected by the value of D_e , see Table 1.

For the optimal morphing parameters, M2 applied to the MRCI+Q PES yields an enlargement of R by $\sim 1 \%$ whereas r_{HH} is reduced by 1.9% and ε remains unaffected. The reduction in r_{HH} leads to a small increase in the height of the barrier between the two wells of the

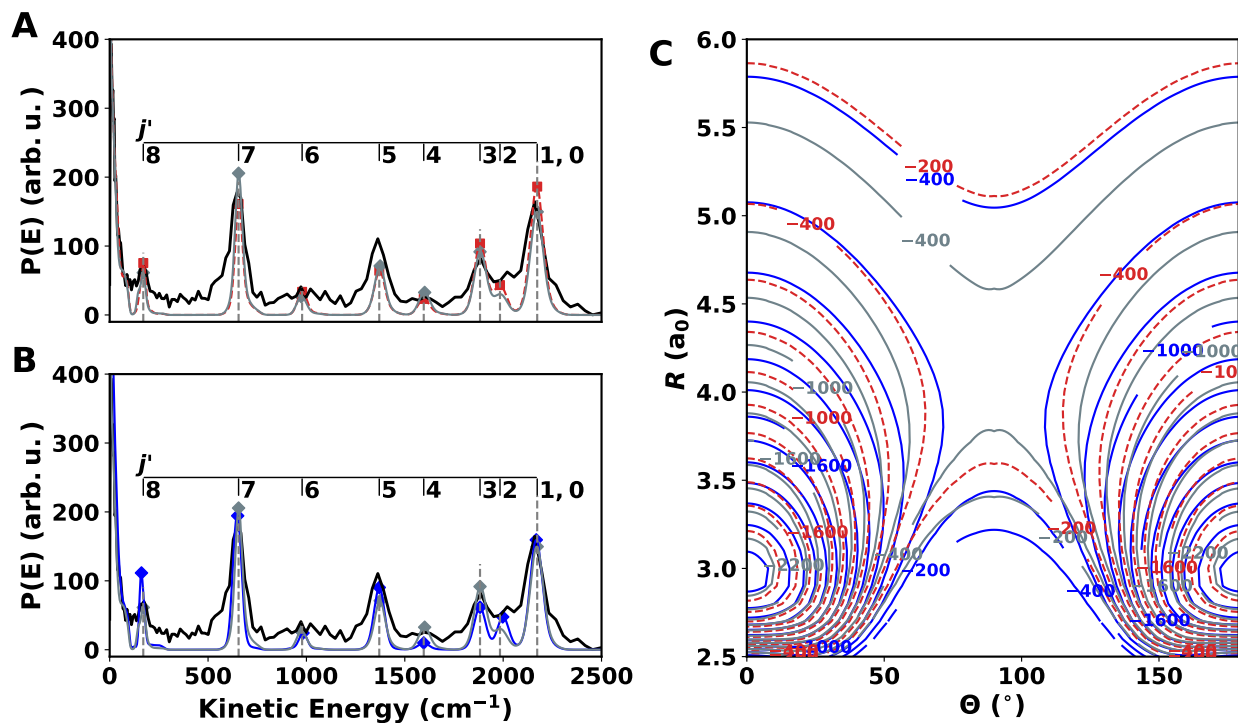


Figure 4: Cross sections (A,C) obtained from experiment (black, data taken from Ref. 23) and full coupled channels calculations using the unmorphed (dashed lines) and M2-morphed (solid lines) PESs (B,D) for MRCI+Q (A,B), and MP2 (C,D). The RMSE for the peak positions and heights are reported in Table 1. The projections of the PES (B,D) are shown for $r = r_e a_0$ (See Table 1) with the zero of energy set for the r -value considered and $R = \infty$. Energies are in cm^{-1} . The changes in the PES suggest that the observables are primarily sensitive to the long-range part and the repulsive wall of the PES.

potential (Figure 4B) and a corresponding increase in the energy of the transition state, as observed in the minimum energy path (MEP), see Figure S14, for the angular coordinate. This effect is compensated by a positive displacement of the values of R (Figure S15) for the MEP. On the other hand, for the MP2 surface, the morphing parameters are (+0.6, +19.0, -0.04) %. The large positive value for β results in a displacement of the H_2^+ bond length to a shorter equilibrium value (Figure S16 and S17). For the R coordinate, the values are also reduced while the barrier height remains unchanged (Figure S15). As for M1, in the MP2 and MRCI+Q PESs the largest changes are observed in the r_{HH} coordinate. However, in the M2 method, scaling of the global PES results in a better performance for the calculation of the observable and a better physical description.

Finally, morphing one PES into another one can probe the flexibility of the morphing transformation as a whole. To this end, the MP2 PES was morphed to best compare with the FCI PES in a least squares sense according to method M2, i.e., by finding parameters $(\alpha, \beta, \varepsilon)$ that minimize $(V_{\text{FCI}}(R, r, \theta) - \varepsilon V_{\text{MP2}}(\alpha R, \beta r, \theta))^2$. This optimization procedure reduces the RMSE between the FCI and unmorphed vs. morphed PES by about 30% (from 138 cm^{-1} to 97 cm^{-1} , see Figure S18). The changes in the topology of the surface in Figure 5C indicate that the morphed MP2 PES is "pulled towards" the FCI PES: Consider, for example, the isocontours for -400 cm^{-1} for which the original MP2 isocontour (blue) is far away from the FCI target contour (red), whereas the morphed PES (grey) is deformed towards the grey target isocontour. Closer inspection reveals this to occur for all the other isocontours in Figure 5C as well. The barrier separating the $[\text{He-HH}]^+$ and $[\text{HH-He}]^+$ minima is reduced, which is also seen in the minimum energy path (see Figure S19).

The results of the scattering calculations performed with the surface from the PES-to-PES morphing procedure (Figure 5A) are overall slightly inferior to those obtained from the initial FCI and MP2 PESs, when compared with the experimental data: a negligible increase of the

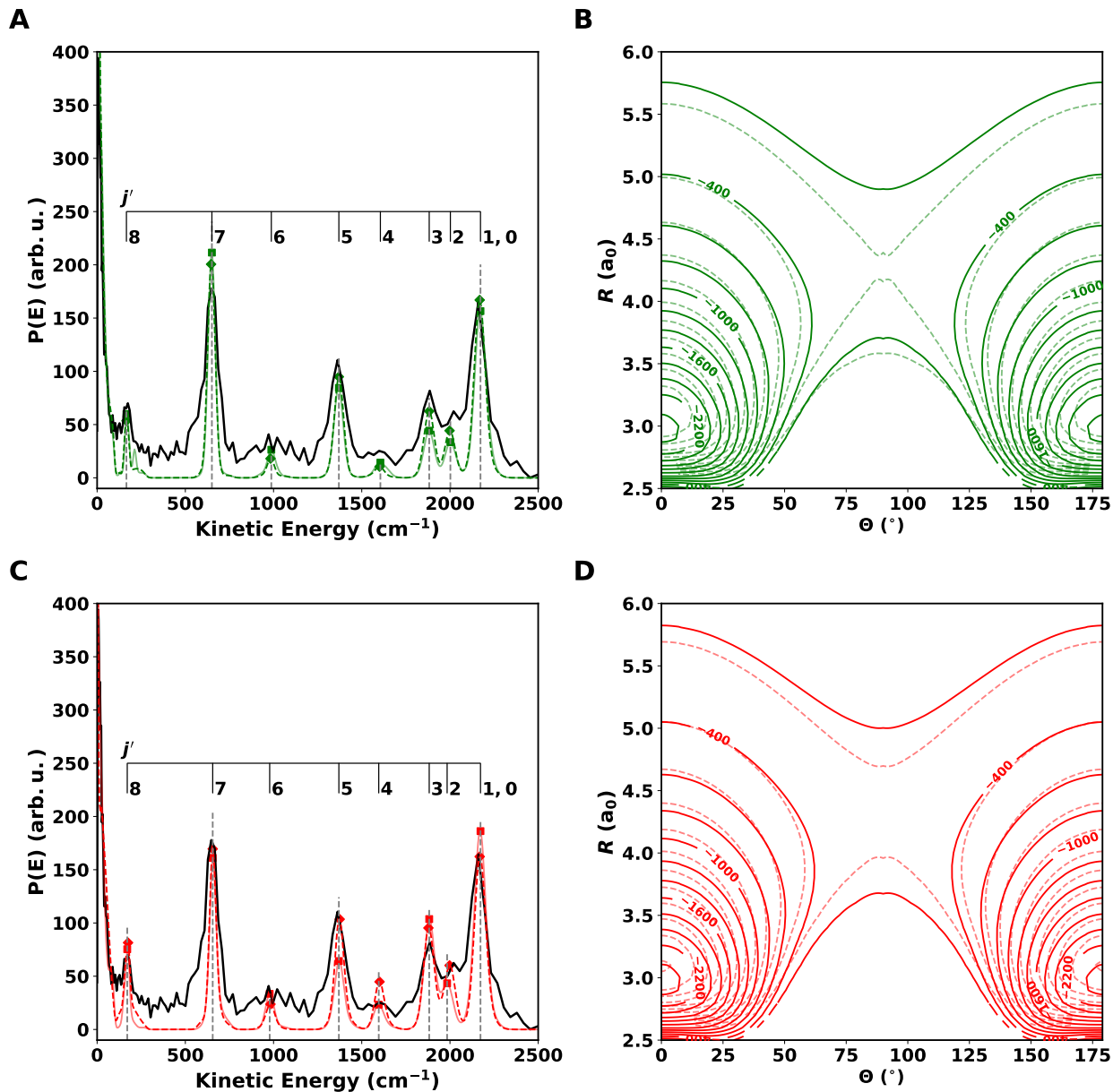


Figure 5: Morphing PES-to-PES. Panel A: Cross-sections obtained from experiments (black, data taken from Ref. 23) and scattering calculations on the unmorphed MP2 (dashed light red) and the morphed (grey) PESs for M2 PES-to-PES morphing procedure with the FCI PES as target. Panel B: Same as Panel A but comparing the best morphed PES (grey) to the unmorphed FCI surface (solid blue). Panel C: 2D projections of the PES for $r = 2.0 a_0$ for unmorphed FCI (solid blue), unmorphed MP2 (dashed light red) and best-morphed PES (grey). The zero of energy is set to the value of the PES at $r_{\text{HH}} = 2.0 a_0$ and $R = \infty$. Energies are in cm^{-1} .

RMSE for the peak positions ($< 1\%$) and intensities (2.2 %) is found. Moreover, the fact that the morphing transformation increases the well depth by merely 10 cm^{-1} indicates that the simple morphing transformation scaling only distances and the energy is not sufficiently flexible to accommodate global changes between topologies as different as FCI vs. MP2.

The results indicate that at all levels of theory improvements in describing the experimental observables are possible. At the same time morphing applied in the fashion done here provides a stringent test to probe the quality of an initial PES at a quantitative level - with higher initial levels of theory, the changes that need to be accommodated decrease and specific deficiencies of a particular quantum chemical approach can be unveiled.

3 Discussion and Outlook

Given that essentially exact quantum calculations are possible for the He-H_2^+ complex,^{20,21,23} the present results highlight what can and cannot be learned about molecular PESs — the central concept in classical and quantum molecular dynamics — from accurate and rather comprehensive experimental data based on Feshbach resonances. One hallmark of such quantum scattering resonances is the large spatial extent of the PES which the resonance wavefunction probes (Figure S20 and discussion in SI). In this regard, the kinetic energy spectrum obtained from the decay of the Feshbach resonances differs from spectroscopic observables, typically involving bound states sensitive to smaller spatial regions of the PES.⁷

In addition to the actual changes of the PES, a comparison of the two morphing procedures employed provides insight into the relationship between the PES, the information provided by specific observables, and how this information can be used to improve an initial PES. First, the much better performance of morphing the global interaction energy instead of

restricting to the three-body contributions reveals the importance of corrections already at the level of two-body interactions. Moreover, the physically meaningful changes to the PES identified by the global morphing concern essentially the anisotropy in the long range. To this end, comparatively small changes of the PESs result in significant improvements in the agreement between calculated and measured observables. This is in line with the expectation that Feshbach resonance wavefunctions mainly probe the anisotropy of the PES in the long-range. Both observations taken together suggest extending the morphing transformation to include higher-order (and nonlinear) terms as well as the angular degree of freedom θ for further improvements.

At a fundamental level, the present findings raise the question how much and what experimental data is required to completely characterize a molecular PES. Indeed, the present work proposes several PESs with comparable average performance on the scattering observables, even though the shapes and local characteristics of the PESs differ greatly, illustrating that the information contained in the Feshbach resonances is not sufficient to uniquely define the PES. In particular, information on the bound-state region is missing. One possible way to answer the question which combination of observables is suited to completely characterize the dynamics of a molecular system has been developed in quantum information science and is referred to as quantum process tomography.²⁶ It has been adapted to molecular systems for example in the context of ultrafast spectroscopy. In future work, quantum process tomography could be applied to the quest of uniquely defining a PES by making use of the mapping between the real-space representation of the molecular Hamiltonian and qubits.²⁷ This should allow for a systematic approach to identify the most important measurements which would then provide additional data for morphing PES.

4 Methods

4.1 Potential Energy Surfaces

For the present work, three PESs were employed. Full-dimensional PESs for He–H₂⁺ were previously determined at the FCI/aug-cc-pV5Z and MRCI+Q/aug-cc-pV6Z levels of theory, respectively.²¹ The reference data was represented as a reproducing kernel Hilbert space (RKHS)^{28,29} which provides a highly accurate interpolation and allows to encode the leading order long-range behaviour for large separations. In addition, a third PES using the same underlying grid for determining reference energies at the MP2/aug-cc-pV5Z level and also represented as a RKHS, was constructed for the present work. These calculations were carried out using the MOLPRO suite of codes.³⁰ All PESs are represented as a sum of diatomic potential energy curves together with an explicit three-body interaction. The complete many-body expansion for the He–H₂⁺ system is given in Eq. (1), where distances $r_i \in \{r_{\text{HeH}}, r_{\text{HeH}^+}, r_{\text{H}_2^+}\}$ in the two-body terms $\mathcal{V}_i^{(2)}$ are the distances between the respective atoms, whereas for the three-body term $\mathcal{V}^{(3)}(R, r, \theta)$ the coordinate r is the H₂⁺ separation $r_{\text{H}_2^+}$, R the distance between He and the centre of mass of the diatomic, and θ the angle between the two distance vectors \vec{r} and \vec{R} . Finally, $\mathcal{V}^{(1)}$ corresponds to the respective atomic energies. The energies $\mathcal{V}_i^{(1)}$ and $\mathcal{V}_i^{(2)}$ were also determined at the respective level of theory from electronic structure calculations and the contributions $\mathcal{V}_i^{(2)}$ were fitted to analytical expressions described in Ref. 21. The fitting parameters for the FCI and MRCI levels of theory were published before and those for the MP2 level of theory are provided in the supporting information. Combining all this information, the three-body contribution $\mathcal{V}^{(3)}(R, r, \theta)$ was obtained on the grid used in the electronic structure calculations for $V(R, r, \theta)$ and represented as a RKHS.

4.2 Scattering calculations

Integral scattering cross sections and scattering wave functions for He-H₂⁺, resulting from a spatially distributed input wave packet, were evaluated using a home-written coupled-channels collision simulation based on the renormalized Numerov method.^{31,32} Details on these calculations have been given in earlier work²³ and only the salient features are presented here. The wavepacket simulations use Jacobi coordinates with \vec{r} the vector between the hydrogen atoms, \vec{R} the vector from the dihydrogen centre of mass to the helium atom and θ the angle between the two vectors. With $R = |\vec{R}|$ and $r = |\vec{r}|$, the total Hamiltonian is then

$$H_{\text{tot}} = -\frac{\hbar^2}{2\mu_{\text{cmplx}}} \nabla_{\vec{R}}^2 - \frac{\hbar^2}{2\mu_{\text{diat}}} \nabla_{\vec{r}}^2 + V(R, r, \theta) , \quad (2)$$

where μ_{cmplx} is the reduced mass of the three-body complex, μ_{diat} the reduced mass of the dihydrogen molecule, and $V(R, r, \theta)$ the three-dimensional PES. The total wavefunction of the system $\Psi(\vec{R}, \vec{r})$ is written as a product of R -, r -, and angularly dependent terms,

$$\Psi^{JMvj\ell}(\vec{R}, \vec{r}) \propto \sum_{v'j'\ell'} G_{v'j'\ell'}^{Jvj\ell}(R) \chi_{\text{diat},v'j'}(r) \sum_{m_j=-j}^j \sum_{m_\ell=-\ell}^{\ell} C_{m_j m_\ell}^{JM} Y_{\ell, m_\ell}(\theta_R, \varphi_R) Y_{j, m_j}(\theta_r, \varphi_r) , \quad (3)$$

see Ref. 23 for more detail. Channels consist of tuples of quantum numbers v, j , and ℓ , corresponding to diatomic vibration, rotation and orbital angular momentum, respectively. In Eq. (3), $\chi_{\text{diat},v,j}(r)$ designates the rovibrational eigenstates of the molecule. Starting from a given entrance channel, the Schrödinger equation is solved numerically to obtain the radial wave functions $G(R)$ for the exit channel with quantum numbers (v', j', ℓ') connected with the entrance channel (v, j, ℓ) . The total angular momentum, $\vec{J}_{\text{tot}} = \vec{j} + \vec{\ell}$ obtained from coupling diatomic and orbital rotation, and parity are conserved under the Hamiltonian (2).

In the experiments, the He-H₂⁺ complex (plus a leaving electron) is formed by Penning ionization (He*+H₂), and the scattering calculations considered in the present work describe

the half-collision on the He–H₂⁺ PES. The initial wavepacket $\phi(R)$ along the R –coordinate is approximated by Gaussian distributions centered around $R \approx 8 a_0$.²³ The experiment prepares the input wavepacket with $j_{\text{wp}} = 0, 1$ for para- and ortho-H₂⁺, respectively. However, as the system is prepared in a superposition of J –states, individual simulations need to be carried out for each possible value of J and partial wave ℓ . Then, the integral cross section is calculated as a weighted sum over the individual contributions for a given collision energy $E_{\text{col}}/k_{\text{B}} \approx 2.5$ K. The J –weights, which were calculated separately,³³ are shown in Figure S21.

Evaluation of the collision cross section due to the spatially distributed input wavepacket can be accomplished by expanding $\phi(R)$ in a basis of eigenfunctions of H_{tot} . To this end, the time-independent Schrödinger equation was solved on a discretized interval of 1002 energies ranging from 100 cm⁻¹ below to 100 cm⁻¹ above the dissociation threshold of the given entrance channel. Because full coupled-channel calculations are computationally demanding, the considered set of initial wavepacket quantum numbers J and ℓ was limited to $(\ell/J) \in \{(0/0), (1/1), (2/2), (3/3), (4/4)\}$ for para- and $(\ell/J) \in \{(0/1), (1/1, 2), (2/1, 2, 3), (3/2, 3, 4), (4/3, 4, 5)\}$ for ortho-dihydrogen, respectively. For each coupled channel calculation a converged basis set of diatomic rotational states up to $j_{\text{max}} = 19$ and diatomic vibrational states up to $v_{\text{max}} = 5$ was used.

Solving the Schrödinger equation in this fashion allows for calculating the channel-resolved integral cross section for each energy in the discretized interval. For a given output channel, the eigenenergy $E_{v'j'\ell'} = E_{\text{int},v'j'\ell'} + E_{\text{kin},v',j',\ell'}$ can be decomposed into its internal and kinetic parts, respectively. By generating a histogram for all output channels (v', j', ℓ') , the cross-section can be expressed as a function of kinetic energy, which can be compared with the experimental results. Next, the kinetic energy histogram is convoluted using a Gaussian envelope to account for the finite resolution in the experiments.²³ Before convolution, and

as shown in Figure S22, the computed peaks are sharp in E_{kin} which is a signature of Feshbach resonances. It should be noted that experimental peaks are clearly distinguishable and energetically match the theoretical predictions. However, the peak shapes and heights can vary, dependent on the histogram resolution and convolution width. In this work, only single initial vibrational excitations ($v = 1$) were considered, in order to exploit the experimental resolution of separate j' peaks in the cross-section as a function of kinetic energy.³⁴

4.3 Morphing

The morphing transformation considered here is

$$V_{\text{morphed}}(R, r, \theta) = \varepsilon V_{\text{ab-initio}}(\alpha R, \beta r, \theta) . \quad (4)$$

In Eq. (4), the three parameters ($\alpha, \beta, \varepsilon$) are used for energy- (ε) and geometry- (α, β) related scalings. For the purpose of this work, the angle θ was not modified. The morphing procedure described further below optimizes the values of ($\alpha, \beta, \varepsilon$) such that the difference between observed and computed features of the resonances is minimized. Application of such a procedure modifies local features (e.g. slope, curvature) of the PES but maintains its global shape.

For morphing M1 and M2 the refinement with respect to experimental values is formulated as an optimization problem with a loss function,

$$\mathcal{L} = \min_{\alpha, \beta, \varepsilon} \left[\sum_{j'} |E_{\text{exp}}^{(j')} - E_{\text{calc}}^{(j')}(\alpha, \beta, \varepsilon)| + \sum_{j'} \delta_{h(j')}^{\kappa} \right] , \quad (5)$$

to be minimized. Here, $E^{(j')}$ is the kinetic energy of each cross-section corresponding to an exit-channel j' , and $\delta_{h(j')}^{\kappa}$ accounts for the difference in the peak heights between experimental

and calculated values:

$$\delta_{h(j')}^\kappa = \begin{cases} (\Delta h(j') - h_{\text{noise}})^\kappa, & (\Delta h(j') - h_{\text{noise}})^\kappa > 0, \\ 0, & (\Delta h(j') - h_{\text{noise}})^\kappa \leq 0, \end{cases} \quad (6)$$

where, $\delta_h(j')$ is *regularized* by subtracting $h_{\text{noise}} = 10.0$ to avoid fitting experimental noise. By design, only values $\delta_h(j') > 0$ contribute to the error. Here $\Delta h(j') = |h_{\text{exp}}^{(j')} - \gamma h_{\text{calc}}^{(j')}(\alpha, \beta, \varepsilon)|$, where $h^{(j')}$ is the peak height of the cross section corresponding to an exit-channel j' . The parameter γ is recalculated after each iteration to best match the experiment by performing an additional 1d minimization over the squared difference in peaks heights.

The workflow to perform the optimization of Eq. (5) is shown schematically in Figure 1. In the first step, *ab initio* points of the PES are used to generate a RKHS kernel. Depending on the morphing procedure chosen, a new RKHS needs to be generated (for M1) or the existing kernel will be reused (for M2). All kernels are constructed and evaluated using the “fast” method.²⁸ The obtained PES is passed to the scattering code to perform the wavepacket propagation. Next, the resulting cross-sections are processed and then compared with the available experimental data. If the difference between experimental and calculated values matches a given tolerance the cycle finishes; otherwise, the PES is modified by three parameters as described in Eq. (4) following the chosen morphing approach. The values of the parameters α , β and ε were obtained by a non-linear optimization using the NLOpt package.³⁵

Data Availability Statement

The data needed for the PESs is available at <https://github.com/MeuwlyGroup/morphing>.

Acknowledgments

This work was supported by the Swiss National Science Foundation grants 200021-117810, 200020-188724, the NCCR MUST, and the University of Basel which is gratefully acknowledged. The authors thank B. Margulis and Prof. E. Narevicius for providing the experimental data used in this work.

References

- (1) Wales, D. J. Exploring Energy Landscapes. *Annu. Rev. Phys. Chem.* **2018**, *69*, 401–425.
- (2) Käser, S.; Vazquez-Salazar, L. I.; Meuwly, M.; Töpfer, K. Neural network potentials for chemistry: concepts, applications and prospects. *Dig. Discov.* **2023**, *2*, 28–58.
- (3) Child, M.; Nesbitt, D. RKR-based inversion of rotational progressions. *Chem. Phys. Lett.* **1988**, *149*, 404–410.
- (4) Nesbitt, D. J.; Child, M. S.; Clary, D. C. Rydberg–Klein–Rees inversion of high resolution van der Waals infrared spectra: An intermolecular potential energy surface for $\text{Ar}^+ \text{HF}(v = 1)$. *J. Chem. Phys.* **1989**, *90*, 4855–4864.
- (5) Nesbitt, D. J.; Child, M. S. Rotational-RKR inversion of intermolecular stretching potentials: Extension to linear hydrogen bonded complexes. *J. Chem. Phys.* **1993**, *98*, 478–486.
- (6) Kurtz, L.; Rabitz, H.; de Vivie-Riedle, R. Optimal use of time-dependent probability density data to extract potential-energy surfaces. *Phys. Rev. A* **2002**, *65*, 032514.
- (7) Meuwly, M.; Hutson, J. M. Morphing ab initio potentials: A systematic study of Ne-HF . *J. Chem. Phys.* **1999**, *110*, 8338–8347.
- (8) Bowman, J. M.; Gazdy, B. A simple method to adjust potential energy surfaces: Application to HCO . *J. Chem. Phys.* **1991**, *94*, 816–817.

- (9) Ramakrishnan, R.; Dral, P. O.; Rupp, M.; Von Lilienfeld, O. A. Big data meets quantum chemistry approximations: the Δ -machine learning approach. *J. Chem. Theor. Comp.* **2015**, *11*, 2087–2096.
- (10) Smith, J. S.; Nebgen, B. T.; Zubatyuk, R.; Lubbers, N.; Devereux, C.; Barros, K.; Tretiak, S.; Isayev, O.; Roitberg, A. E. Approaching coupled cluster accuracy with a general-purpose neural network potential through transfer learning. *Nat. Commun.* **2019**, *10*, 1–8.
- (11) Käser, S.; Meuwly, M. Transfer learned potential energy surfaces: accurate anharmonic vibrational dynamics and dissociation energies for the formic acid monomer and dimer. *Phys. Chem. Chem. Phys.* **2022**, *24*, 5269–5281.
- (12) Thaler, S.; Zavadlav, J. Learning neural network potentials from experimental data via Differentiable Trajectory Reweighting. *Nat. Comm.* **2021**, *12*, 6884.
- (13) Yurchenko, S. N.; Lodi, L.; Tennyson, J.; Stolyarov, A. V. Duo: A general program for calculating spectra of diatomic molecules. *Comput. Phys. Commun.* **2016**, *202*, 262–275.
- (14) Lorenz, K. T.; Westley, M. S.; Chandler, D. W. Rotational state-to-state differential cross sections for the HCl–Ar collision system using velocity-mapped ion imaging. *Phys. Chem. Chem. Phys.* **2000**, *2*, 481–494.
- (15) Vargas-Hernández, R.; Guan, Y.; Zhang, D.; Krems, R. Bayesian optimization for the inverse scattering problem in quantum reaction dynamics. *New J. Phys.* **2019**, *21*, 022001.
- (16) van Mourik, T.; Harris, G. J.; Polyansky, O. L.; Tennyson, J.; Császár, A. G.; Knowles, P. J. Ab initio global potential, dipole, adiabatic, and relativistic correction surfaces for the HCN–HNC system. *J. Chem. Phys.* **2001**, *115*, 3706–3718.

- (17) Adhikari, S.; Baer, M.; Sathyamurthy, N. HeH_2^+ : structure and dynamics. *Int. Rev. Phys. Chem.* **2022**, *41*, 49–93.
- (18) Carrington, A.; Gammie, D. I.; Shaw, A. M.; Taylor, S. M.; Hutson, J. M. Observation of a microwave spectrum of the long-range $\text{He} \dots \text{H}_2^+$ complex. *Chem. Phys. Lett.* **1996**, *260*, 395–405.
- (19) Gammie, D. I.; Page, J. C.; Shaw, A. M. Microwave and millimeter-wave spectrum of the $\text{He} \dots \text{H}_2^+$ long-range complex. *J. Chem. Phys.* **2002**, *116*, 6072.
- (20) Asvany, O.; Schlemmer, S.; van der Avoird, A.; Szidarovszky, T.; Császár, A. G. Vibrational spectroscopy of H_2He^+ and D_2He^+ . *J. Mol. Struct.* **2021**, *377*, 111423.
- (21) Koner, D.; Veliz, J. C. S. V.; van der Avoird, A.; Meuwly, M. Near dissociation states for H_2^+-He on MRCI and FCI potential energy surfaces. *Phys. Chem. Chem. Phys.* **2019**, *21*, 24976–24983.
- (22) Kedziera, D.; Rauhut, G.; Császár, A. G. Structure, energetics, and spectroscopy of the chromophores of HHe_n^+ , H_2He_n^+ , and He_n^+ clusters and their deuterated isotopologues. *Phys. Chem. Chem. Phys.* **2022**, *24*, 12176–12195.
- (23) Margulis, B.; Horn, K. P.; Reich, D. M.; Upadhyay, M.; Kahn, N.; Christianen, A.; van der Avoird, A.; Groenenboom, G. C.; Koch, C. P.; Meuwly, M. et al. Tomography of Feshbach resonance states. *Science* **2023**, *380*, 77–81.
- (24) Chin, C.; Grimm, R.; Julienne, P.; Tiesinga, E. Feshbach resonances in ultracold gases. *Rev. Mod. Phys.* **2010**, *82*, 1225.
- (25) Pérez Ríos, J. *Introduction to Cold and Ultracold Chemistry: Atoms, Molecules, Ions and Rydbergs*; Springer, 2020.
- (26) Nielsen, M. A.; Chuang, I. L. *Quantum computation and quantum information*; Cambridge university press, 2010.

- (27) Ollitrault, P. J.; Miessen, A.; Tavernelli, I. Molecular Quantum Dynamics: A Quantum Computing Perspective. *Accounts of Chemical Research* **2021**, *54*, 4229–4238.
- (28) Unke, O. T.; Meuwly, M. Toolkit for the Construction of Reproducing Kernel-Based Representations of Data: Application to Multidimensional Potential Energy Surfaces. *J. Chem. Inf. Model* **2017**, *57*, 1923–1931.
- (29) Ho, T.-S.; Rabitz, H. A general method for constructing multidimensional molecular potential energy surfaces from ab initio calculations. *J. Chem. Phys.* **1996**, *104*, 2584.
- (30) Werner, H.-J.; Knowles, P. J.; Knizia, G.; Manby, F. R.; Schütz, M., et al. MOLPRO, version 2019.2, a package of ab initio programs. 2019.
- (31) Johnson, B. R. The renormalized Numerov method applied to calculating bound states of the coupled-channel Schroedinger equation. *J. Chem. Phys.* **1978**, *69*, 4678–4688.
- (32) Gadéa, F. X.; Berriche, H.; Roncero, O.; Villarreal, P.; Barrio, G. D. Nonradiative lifetimes for LiH in the A state using adiabatic and diabatic schemes. *J. Chem. Phys.* **1997**, *107*, 10515–10522.
- (33) Pawlak, M.; Shagam, Y.; Klein, A.; Narevicius, E.; Moiseyev, N. Adiabatic variational theory for cold atom–molecule collisions: Application to a metastable helium atom colliding with ortho-and para-hydrogen molecules. *J. Phys. Chem. A* **2017**, *121*, 2194–2198.
- (34) Margulis, B.; Narevicius, J.; Narevicius, E. Direct observation of a Feshbach resonance by coincidence detection of ions and electrons in Penning ionization collisions. *Nat. Comm.* **2020**, *11*, 3553.
- (35) Johnson, S. G. The NLOpt nonlinear-optimization package. <http://github.com/stevengj/nlopt>, Accessed: 2021-10-15.

- (36) de Fazio, D.; de Castro-Vitores, M.; Aguado, A.; Aquilanti, V.; Cavalli, S. The He + H₂⁺ → HeH⁺ + H reaction: Ab initio studies of the potential energy surface, benchmark time-independent quantum dynamics in an extended energy range and comparison with experiments. *J. Chem. Phys.* **2012**, *137*, 244306.
- (37) Aguado, A.; Paniagua, M. A New Functional form to Obtain Analytical Potentials of Triatomic Molecules. *J. Chem. Phys.* **1992**, *96*, 1265–1275.
- (38) Falcetta, M. F.; Siska, P. E. The interaction between He and H₂⁺: anisotropy, bond length dependence and hydrogen bonding. *Mol. Phys* **1999**, *97*, 117–125.
- (39) Bishop, D. M.; Pipin, J. Static electric properties of H and He. *Chem. Phys. Lett.* **1995**, *236*, 15.
- (40) Vellilla, L.; Lepetit, B.; Aguado, A.; Beswick, A.; Paniagua, M. The H₃⁺ rovibrational spectrum revisited with a global electronic potential energy surface. *J. Chem. Phys.* **2008**, *129*, 084307.
- (41) Coxon, J. A.; Hajigeorgiou, P. G. Experimental Born–Oppenheimer Potential for the X¹Σ⁺ Ground State of HeH⁺: Comparison with the Ab Initio Potential. *J. Mol. Struct.* **1999**, *193*, 306–318.
- (42) Dinelli, B. M.; Le Sueur, C. R.; Tennyson, J.; Amos, R. D. Ab initio ro-vibrational levels of H₃⁺ beyond the Born-Oppenheimer approximation. *Chem. Phys. Lett.* **1995**, *232*, 295–300.
- (43) Balakrishnan, A.; Smith, V.; Stoicheff, B. Dissociation energy of the hydrogen molecule. *Phys. Rev. Lett.* **1992**, *68*, 2149.
- (44) Roy, R. L. LEVEL 7.5: a Computer Program to Solve the Radial Schrödinger Equation for Bound and Quasibound Levels. 2002.

S1 Two-body potential fitting

In this work, the two-body interaction energy for a molecule AB was expressed as^{21,36,37}

$$\mathcal{V}_{AB}^{(2)}(R_{AB}) = \frac{c_0 e^{-\alpha_{AB} R_{AB}}}{R_{AB}} + \sum_{i=1}^M C_i \rho_{AB}^i + \mathcal{V}_{long}(\tilde{r}) \quad (\text{S7})$$

In equation S7, C_i are linear coefficients with $C_0 > 0$ to assure that the diatomic potential remains repulsive ($V_{AB}(r_{AB}) \rightarrow \infty$) for $r_{AB} \rightarrow 0$ and ρ_{AB}^i is defined as:

$$\rho_{AB}^i = R_{AB} e^{-\beta_{AB}^{(2)} R_{AB}} \quad (\text{S8})$$

The long range part of equation S7 is written as:³⁸

$$\mathcal{V}_{long}(\tilde{r}) = -\frac{\alpha_d q^2}{2\tilde{r}^4} - \frac{\alpha_q q^2}{2\tilde{r}^6} - \frac{\alpha_o q^2}{2\tilde{r}^8} - \frac{\beta_{ddq} q^3}{6\tilde{r}^7} - \frac{\gamma_d q^4}{24\tilde{r}^8} \quad (\text{S9})$$

In equation S9, q is the charge, α_i , $i \in \{d, q, o\}$ are the dipole, quadrupole and octupole polarizabilities for H and He atoms, respectively, and β_{ddq} and γ_d are the first and second hyperpolarizabilities, respectively. Values for these parameters were taken from Refs. 38,39. Finally, the coordinate \tilde{r} , whose objective is to remove the divergence of the long-range terms at short separations of H-H and H-He, is defined as⁴⁰

$$\tilde{r} = r + r_l \exp(-(r - r_e)) \quad (\text{S10})$$

Here, r_l is a distance parameter, and r_e is the equilibrium bond distance of the diatomic molecule. The linear coefficients C_i and the parameters α_{AB} and $\beta_{AB}^{(2)}$ in equations S9 and S8 were taken from Ref. 21 for FCI and MRCI potentials. For the MP2 potential, the values were determined using the same method as described in Ref. 21 and are given in Table S2.

Table S2: Coefficients for the MP2/aug-cc-pV5Z diatomic potentials.

Coefficients	H ₂ ⁺	HeH ⁺
C ₀	1.01921689	10.7720718
α	1.64361518	2.37373920
C ₁	-0.73449753	-4.46348296
C ₂	5.10324938	59.1487168
C ₃	-81.5643228	-3857.67751
C ₄	847.329344	104277.881
C ₅	-5377.78872	-1890643.12
C ₆	21730.0685	21015000.8
C ₇	-56454.3034	-1.3583E+08
C ₈	91470.4779	4.1364E+08
C ₉	-84131.3637	-29244093.5
C ₁₀	33516.3571	-2.0736E+09
β	0.99789130	2.23414441

S2 Discussion of morphing M1 for MRCI and MP2 PESs

Multi-Reference CI: Figure 2B compares the cross sections from experiments with the results from computations with PESs before and after morphing M1 for the MRCI+Q PES. Overall, the RMSE for the energies changes from 10.3 to 12.2 cm⁻¹, whereas the intensities improve from an RMSE of 23.9 to 21.9 arb. u. The results indicate that M1 has the most pronounced impact on intermediate values of j' (i.e. $j' = 4, 5$); see Figures 2D and E. Changes in the peak energies do not show a clear trend. The largest improvements are observed for $j' = 5$ and for $j' = [0, 1]$. Errors for peaks with $j' = 8$ and $j' = 6$ do not reduce using M1. The remaining peaks showed an increase in the error after applying M1. For the peak intensity, again, the largest improvement is observed for the $j' = [0, 1]$ peak. For most other peaks, with the exception of $j' = 5$ and $j' = 8$, there is clearly an improvement in the intensities.

The initial and morphed MRCI PESs are compared in Figure 3B. In this case, morphing increases the anisotropy at long-range compared to the initial PES. However, changes are more pronounced than for the FCI PES. One-dimensional cuts along the r_{HH} and R coordinates

for given angle θ are provided in Figures S23 and S24. As for the FCI PES, the difference between the initial surface and the morphed surface are more pronounced as r_{HH} increases. The 1D cuts of the surface at different values of r_{HH} (Figure S24) show further evidence of the change in the depth of the potential well. The modifications of the energy curves with respect to the r_{HH} coordinate follow the same trend as the FCI surface.

MP2: The results for the lowest-quality surface (MP2) are shown in Figures 2C and 3C. The RMSE for the energies improves from 13.1 to 12.8 cm^{-1} whereas for the intensities, it changes from 22.4 to 10.9 arb. u. Particularly notable is the improvement in the intensities by more than a factor of two. Overall, the changes in the position of the energies and the intensities of the peaks for the calculated cross sections are more pronounced than for the FCI and MRCI+Q PESs. The energy position for peaks with large j' ($j' = 7$ and $j' = 8$) improve by $\approx 5 \text{ cm}^{-1}$. Another difference is that the shoulder of the peak at $j' = 8$ that appears for the two previously described surfaces is not visible for the MP2 surface. For the peaks with $j' = 4$ and $j' = 5$, the error with respect to the experimental spectra upon morphing increases slightly.

The original MP2 PES and its morphed variant for a H_2^+ separation of $r_{\text{HH}} = 2.0 a_0$ are reported in Figure 3C. Because Møller-Plesset second-order theory is a single-reference method and makes further approximations, the changes in the topology of the PES are considerably larger than for the FCI and MRCI+Q PESs. Most of the isocontours are compressed compared with the initial MP2 surface, and the well depth is reduced from 2493 cm^{-1} to 1684 cm^{-1} (Table 1), see Figure S25. The one-dimensional cuts along the r_{HH} and R coordinates for given θ , see Figures S26 and S27, show that as r_{HH} increases the single-reference assumption of the method, leading to convergence problems for small R . As a consequence of the contraction of the potential wells, the barrier of the transition state at $\theta \approx 90^\circ$ is increased, which is further confirmed by the Minimum Energy Path (MEP) shown in Figure S28C. A

more detailed analysis of the MEP (Figure S29C) reveals a small increase in the energy of the transition state along the angular coordinate θ . On the other hand, for the R -coordinate a non-physical barrier emerges at around $3.5 a_0$.

S3 Resonances under Morphing

The cross sections depending on the binding energy between He and H_2^+ as opposed to the relative kinetic energy of the two reactants shows distinct peaks that are no longer separated by final states (j') of the H_2^+ fragment but rather appear as one or several Feshbach Resonances per input J and ℓ at certain values of the binding energy. Both the energy at which a Feshbach Resonance appears, and the distribution of intensities in all exit channels, depend sensitively on the topography of the PES. In consequence, the effect of morphing on the PES can influence the number, energy and intensities of the Feshbach resonances. To illustrate this, it is instructive to consider projections of wave functions for particular resonances to characterize how changes in the PES, which lead to changes in the collision cross-section, are reflected in the radial and angular behaviour of the wave function.

Figure S20 shows the square of the ($v' = v$) and ($j' = j$) components of the resonance wave functions (first and third rows of panels) and corresponding resonances in the cross-section (second and fourth rows of panels) for the dominant ℓ and J contributions for para- and ortho- H_2^+ for all three unmorphed and morphed PESs, respectively. The number, position(s) and intensities of the spectroscopic features respond to morphing in a largely unpredictable way. As an example, the unmorphed and morphed PESs at the FCI level are considered for para- H_2^+ with ($\ell = 4, J = 4$) (left column, rows 1 and 2 in Figure S20). Although M1 changes the topology of the morphed PES only in a minor fashion, the effect on the wavefunctions and resulting spectroscopic feature is clearly visible. For the unmorphed FCI PES there is one resonance at -8.1 cm^{-1} which splits into two resonances at -2.1 cm^{-1} and -16.3 cm^{-1} of approximately equal height upon morphing the PES. Accordingly, the wavefunctions also differ, in particular in the long-range part, i.e. for large R . Similar observations were made for the wavefunctions on the MP2 PES, whereas for the MRCI PESs the changes in the wavefunctions are comparatively smaller.

Conversely, for ortho- H_2^+ the resonances of both FCI and MRCI PESs are affected in a comparable fashion and more noticeable changes to the resonance wave function are observed than for para- H_2^+ . Whilst the resonance wave functions are shifted to larger R in the cases of FCI and MP2, the MRCI resonance wave function only experiences a small shift. Significantly, even though the anisotropy of the PESs only changes in a minor fashion under morphing, all three resonance wave functions respond owing to a change in the superposition of outgoing partial wave (quantum number ℓ'). For the FCI and MP2 PESs angular/radial coupling is enhanced by morphing, which leads to elongation of certain lobes in the wavefunctions along the (R, θ) -direction for ortho- H_2^+ -He. This contrasts with para- H_2^+ -He for which unique assignments of the ro-vibrational quantum numbers is possible from conventional node-counting.

S4 Figures

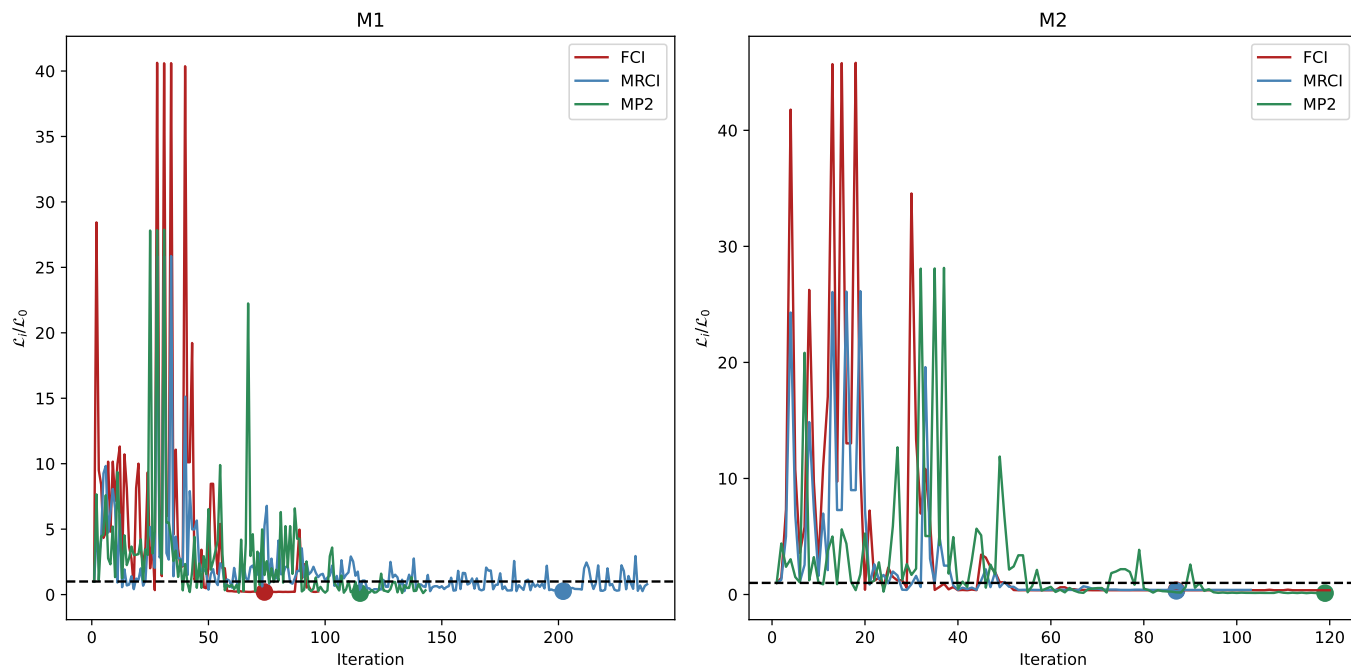


Figure S6: Evolution of the values of the loss function (\mathcal{L}_i) over the iterations with respect to the initial value (\mathcal{L}_0) for the M1(left) and M2 (right) methods. The loss function is defined in the main manuscript.

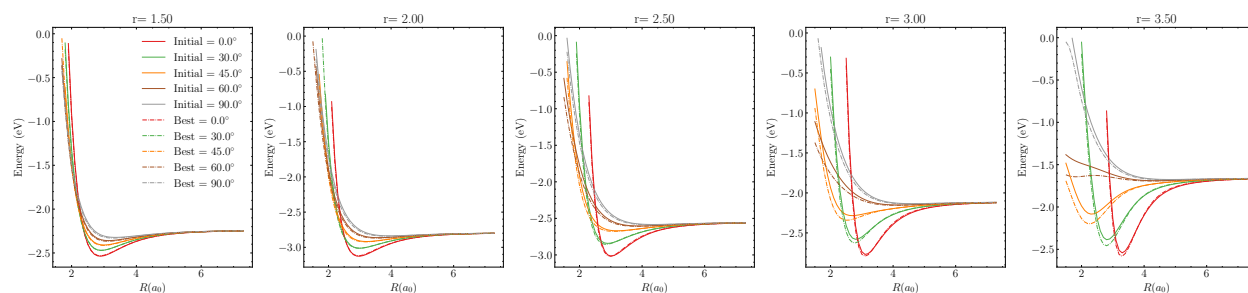


Figure S7: 1D cuts of the FCI PES obtained from the M1 procedure along R for fixed r_{HH} and different angles (θ).

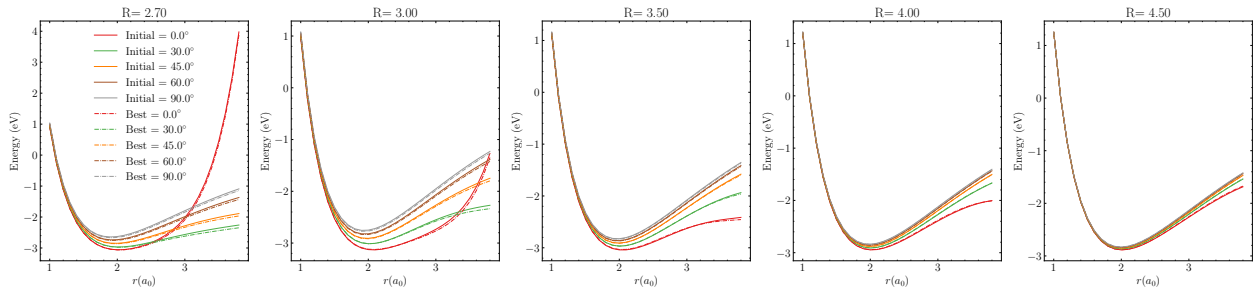


Figure S8: 1D cuts of the FCI PES obtained from the M1 procedure along r_{HH} for fixed R and different angles (θ).

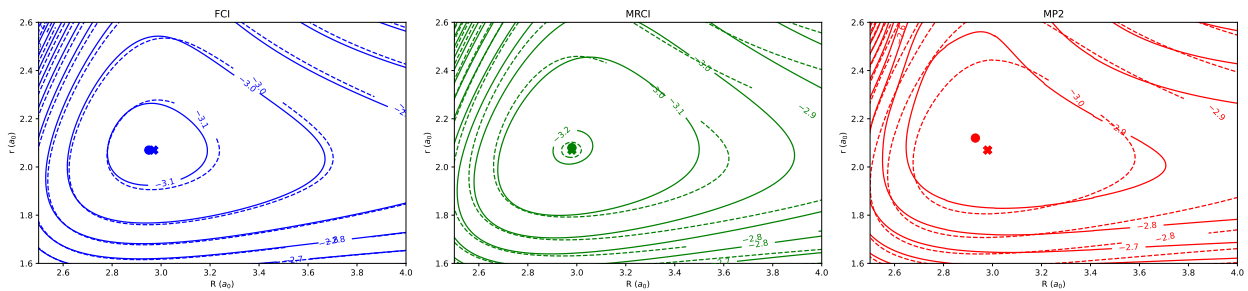


Figure S9: Potential energy surface 2D projection $V(R, r)$ at $\theta = 0^\circ$ obtained from the M1 procedure for the three potentials studied in this work. The dotted lines represent the unmorphed potential, complementary full lines show the morphed potential. Isocontours are separated by 0.1 eV. The minimum of the potential is indicated with a dot and a cross for the unmorphed and morphed potential.

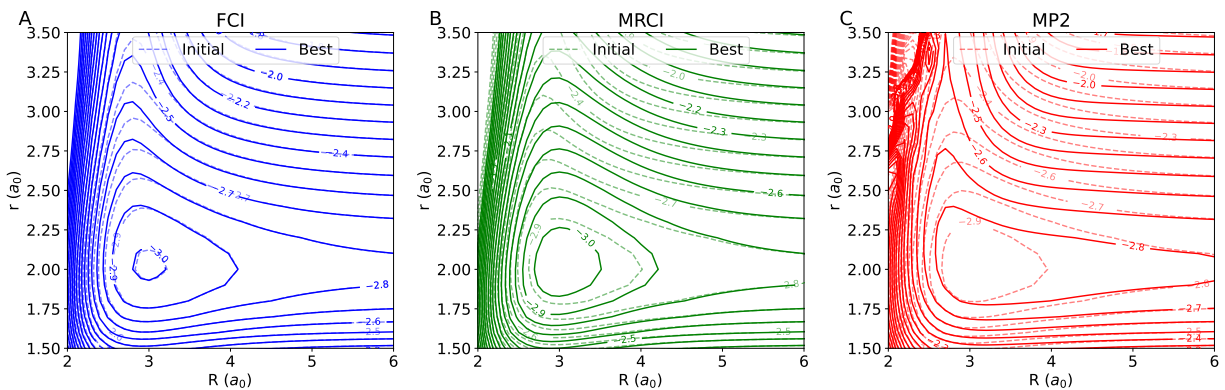


Figure S10: Potential energy surface 2D projection $V(R, r)$ at $\theta = 30^\circ$ obtained from the M1 procedure for the three potentials studied in this work. The dotted lines represent the unmorphed potential; complementary full lines show the morphed potential. Isocontours are separated by 0.1 eV.

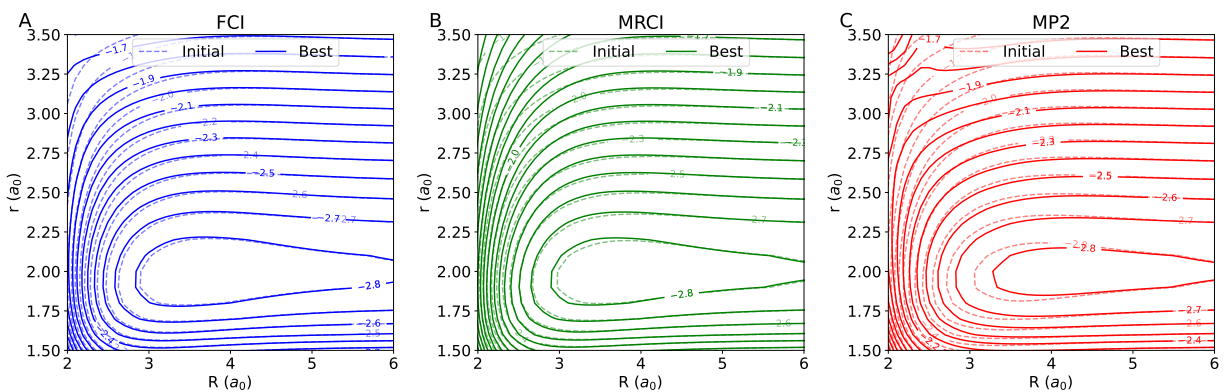


Figure S11: Potential energy surface 2D projection $V(R, r)$ at $\theta = 60^\circ$ obtained from the M1 procedure for the three potentials studied in this work. The dotted lines represent the unmorphed potential; complementary full lines show the morphed potential. Isocontours are separated by 0.1 eV.

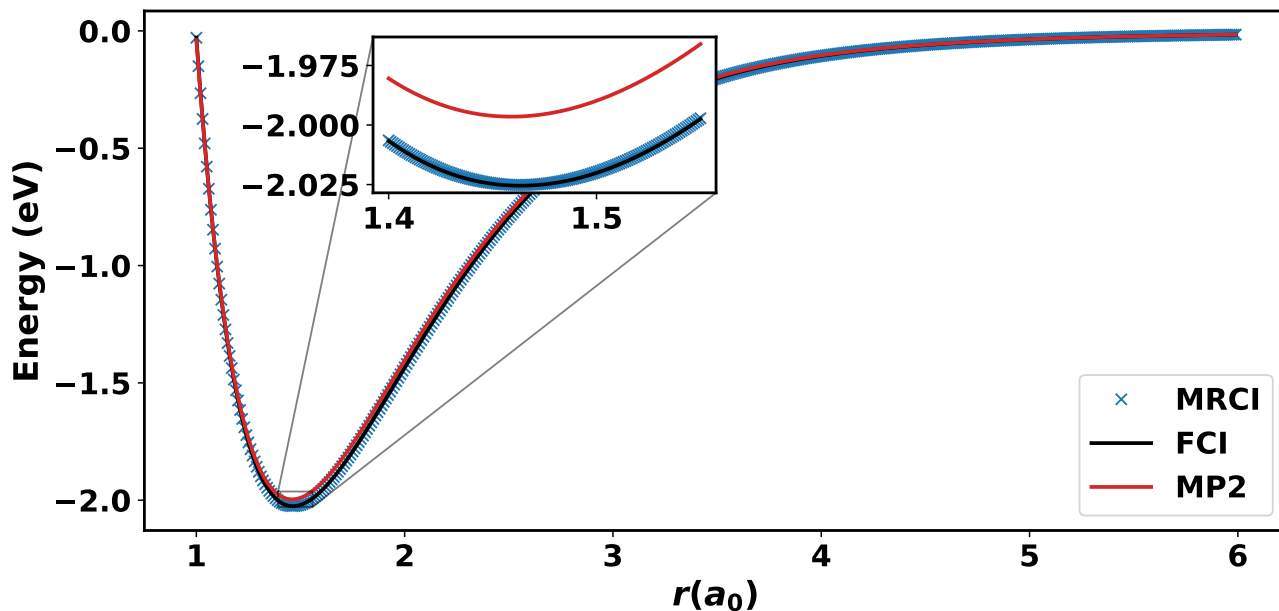


Figure S12: 2-body potential for the HeH^+ molecule. The inset shows the region close to the equilibrium geometry. Zero of energy is at the $\text{He}+\text{H}^+$ asymptote. For HeH^+ the experimentally determined⁴¹ dissociation energy is $D_e = 16456.23 \text{ cm}^{-1}$ compares with 16406.04 (FCI), 16403.96 (MRCI+Q), and 16171.65 (MP2) cm^{-1} from the fitted 2-body potentials. The difference of 235 cm^{-1} between FCI and MP2 is substantial. Remaining differences between experiment and FCI are due to basis set incompleteness and non-Born-Oppenheimer effects, not included in the calculations. For other systems, such effects have been estimated at several ten up to 100 cm^{-1} on total energies.⁴²

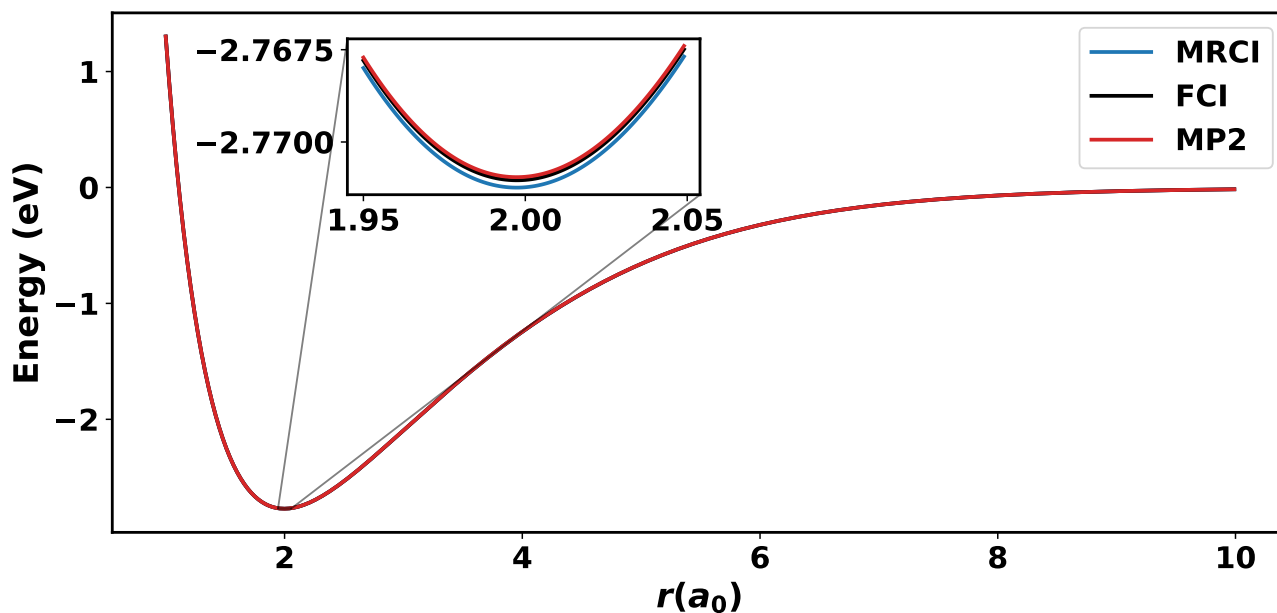


Figure S13: 2-body potential for the H_2^+ molecule. The zero of energy is the $\text{H}+\text{H}^+$ asymptote and the inset shows the region close to the equilibrium geometry. The experimentally determined⁴³ dissociation energy $D_0 = 21379.36 \pm 0.08 \text{ cm}^{-1}$ compares with 21428.5 (FCI), 21430.1 (MRCI+Q), and 21427.5 (MP2) cm^{-1} . The location of the ground states ($v = 0, j = 0$) was determined using the LEVEL code.⁴⁴ Remaining differences between experiment and FCI are due to basis set incompleteness and non-Born-Oppenheimer effects, not included in the calculations. For other systems, such effects have been estimated at several ten up to 100 cm^{-1} on total energies.⁴²

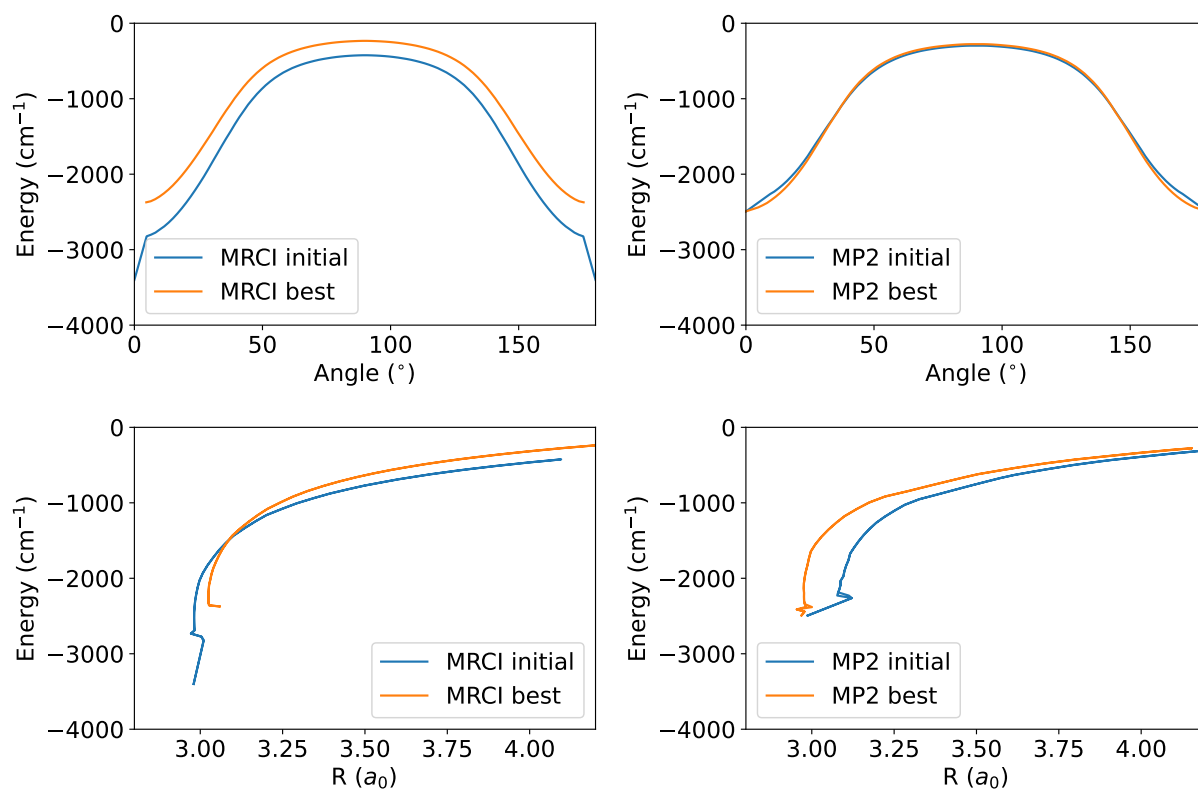


Figure S14: Minimum energy paths (MEPs) for the different surfaces obtained from the M2 method with respect to the variables θ and R . The zero of energy of the path is the energy of the separated monomers.

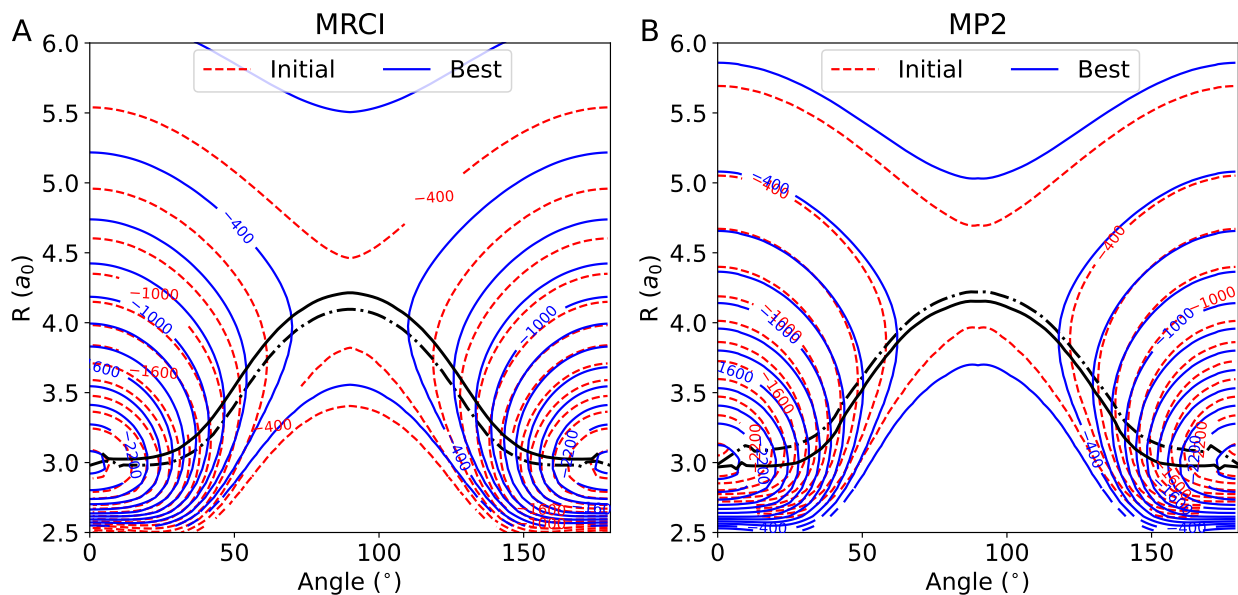


Figure S15: Minimum energy paths (MEPs) for the different surfaces studied before and after applying the morphing M2 method. In solid black, it is shown the MEP for the morph PES. In dotted black, the MEP is shown for the initial PES.

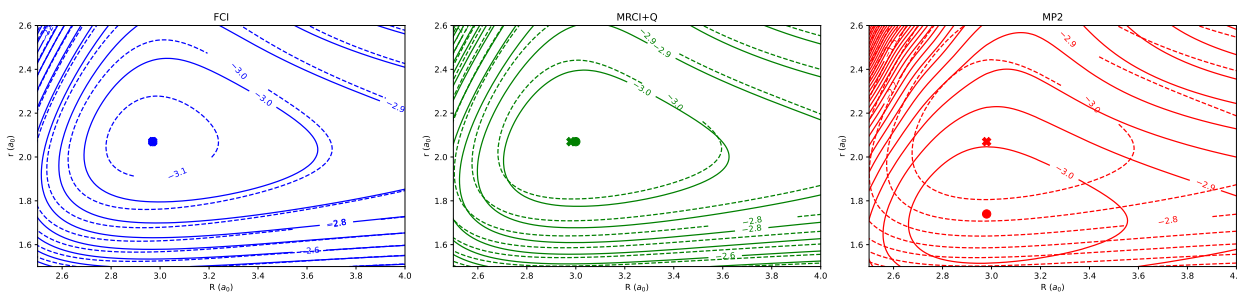


Figure S16: Potential energy surface 2D projection $V(R, r)$ at $\theta = 0^\circ$ obtained from the M2 procedure for the three potentials studied in this work. The dotted lines represent the unmorphed potential. Complementary full lines show the morphed potential. Isocontours are separated by 0.1 eV. The minimum of the potential is indicated with a dot and a cross for the unmorphed and morphed potential.

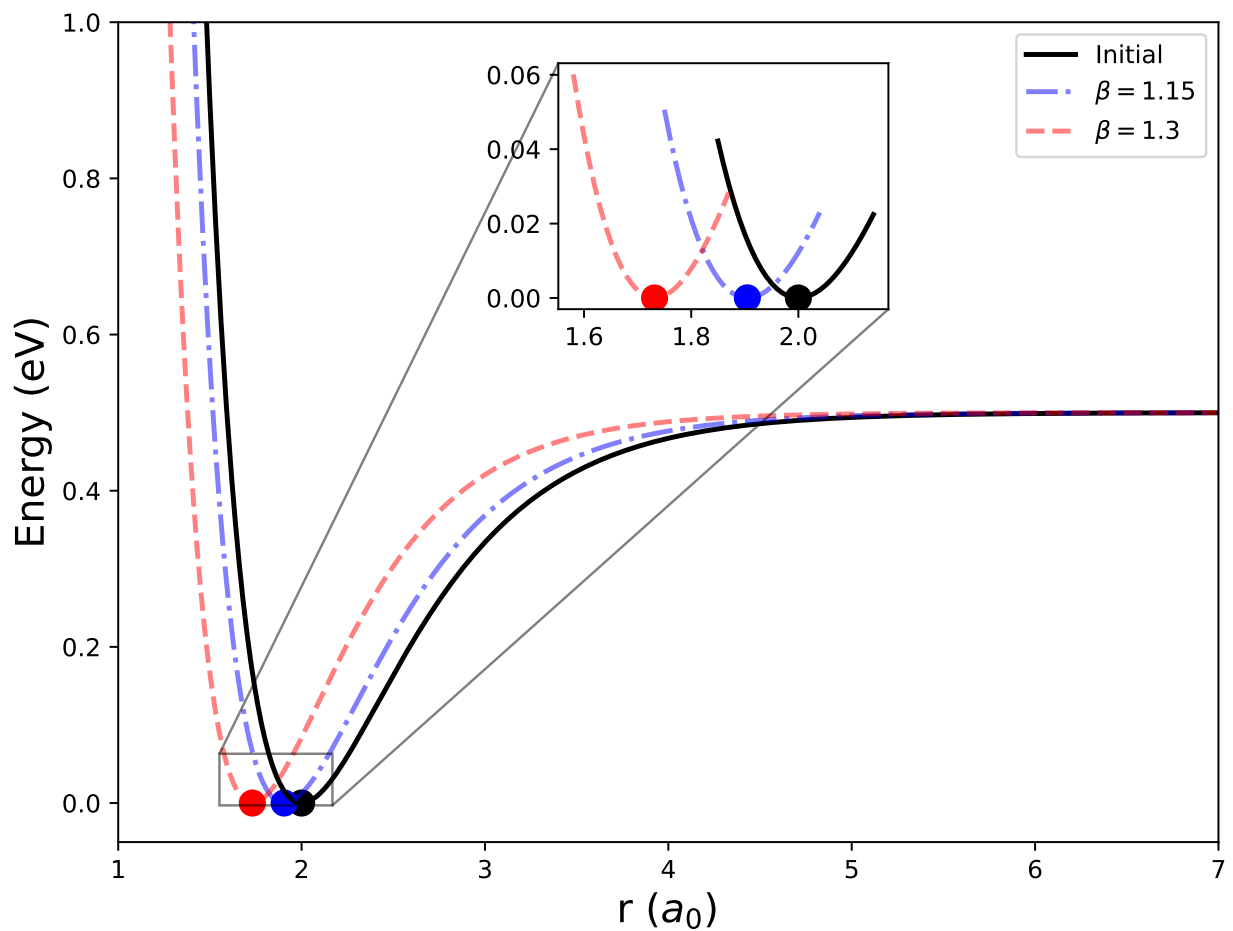


Figure S17: Schematic representation of the changes in the geometry by the morphing transformation for an example Morse potential curve. If the value of the scaling parameter $\beta > 1$, the equilibrium minima will be displaced to smaller values of coordinate r . The insight shows the change in the curvature close to the value of the equilibrium geometry

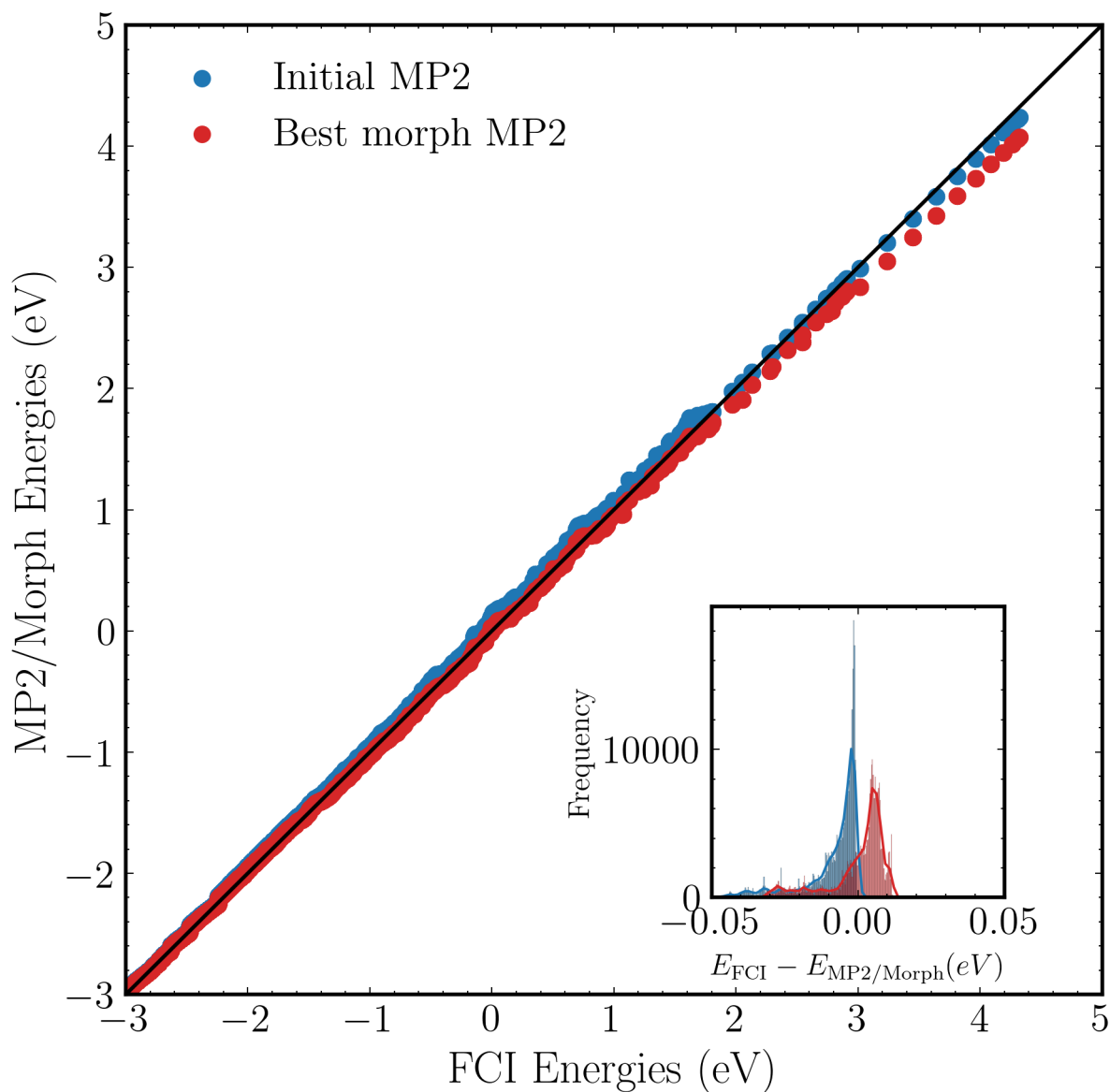


Figure S18: Scatter plot of the energies of the FCI surface vs the initial and morphed MP2 surface for the PES-to-PES procedure. In the inset of the figure, the distribution of differences $E_{\text{FCI}} - E_{\text{MP2}}$ for unmorphed and morphed MP2 surfaces, respectively. The Pearson correlation coefficients are 0.9984 and 0.9988 for unmorphed and morphed MP2 PESs and the RMSE decreases from 138 cm^{-1} to 87 cm^{-1} upon morphing for energies spanning $\sim 7 \text{ eV}$.

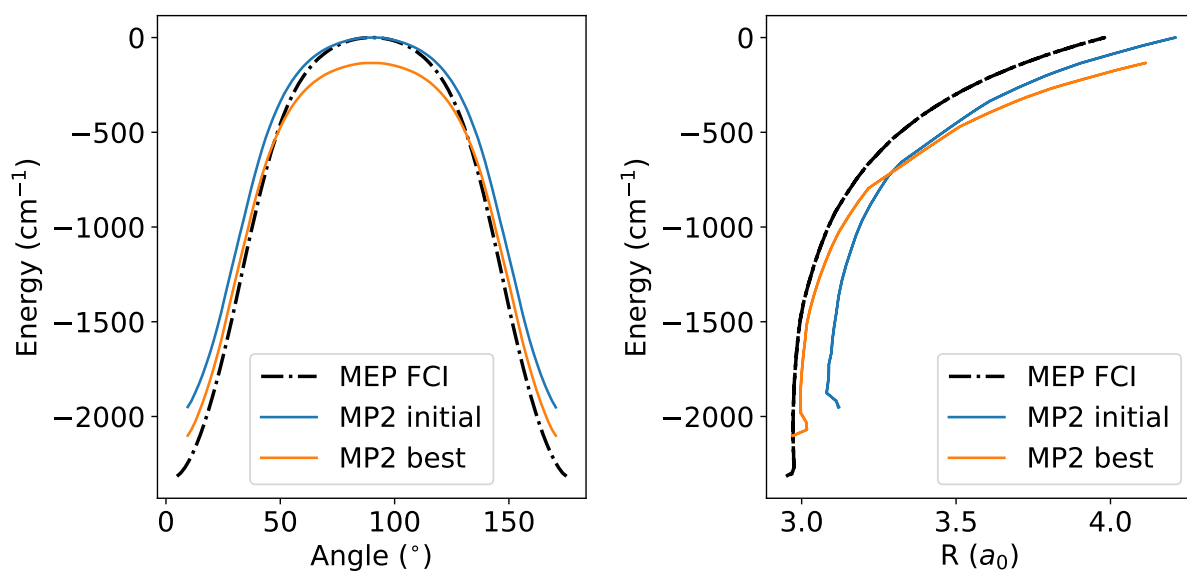


Figure S19: Minimum energy paths (MEPs) for the morph between the FCI and MP2 surface (PES to PES morphing) with respect to the variables θ and R . In black, the MEP for the FCI surface used as reference. The zero of energy of the path was chosen as the energy of the transition state for the unmorphed potential.

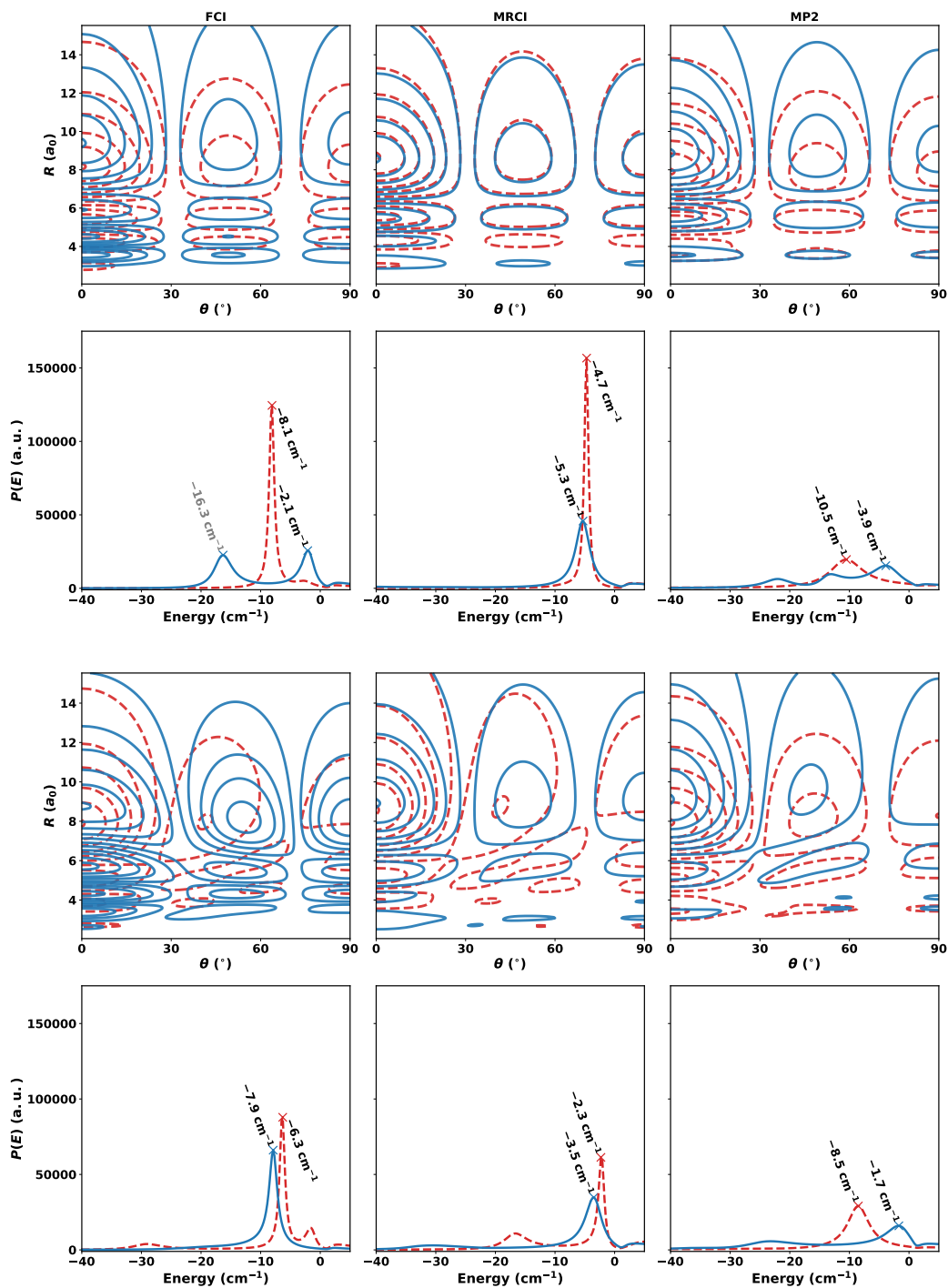


Figure S20: Comparison of the unmorphed (red, dotted) and morphed (blue) absolute value squared resonance wave functions in two dimensions (R, θ) in the case of para-H₂⁺ $\ell = 4, J = 4$ (upper two rows) and ortho-H₂⁺ $\ell = 4, J = 5$ (lower two rows) for resonance energies as marked and labelled in the corresponding cross sections are shown as a function of binding energy (second and fourth rows for para and ortho, respectively). The resonance wave functions have been scaled to have a maximal value of one, and the contours occur at 0.01, 0.1, 0.25, 0.5, 0.75 and 0.99.

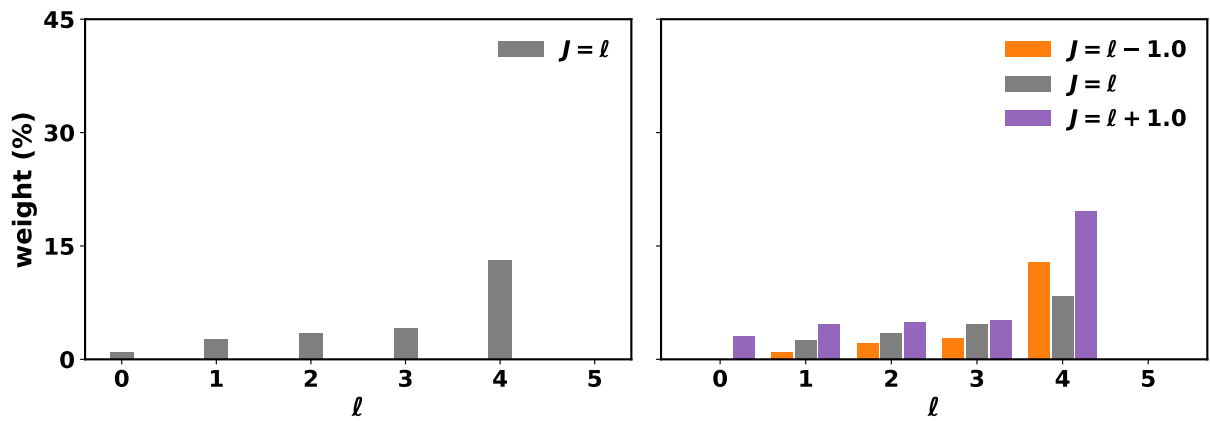


Figure S21: Relative contribution of each angular momentum state for collision of He(³P) with para- and ortho-H₂ (left and right panels, respectively) for the experimental collision energy $E_{\text{col}}/k_{\text{B}} \approx 2.5\text{K}$ and spread. Note that contributions for $\ell > 5$ are not shown since they are negligibly small.

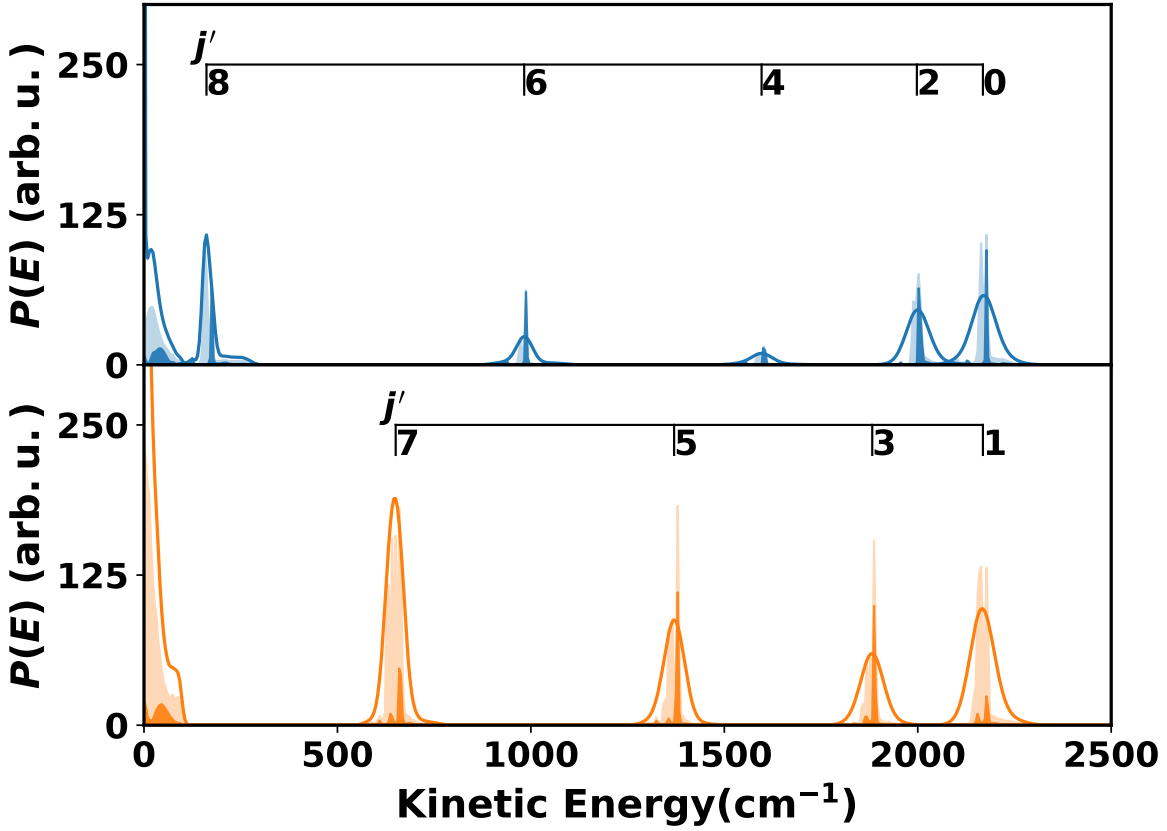


Figure S22: Theoretical kinetic energy histograms for para (above) and ortho (below) H_2^+ in their convoluted (line) and unconvoluted (shaded area) forms. The unconvoluted cross-sections have been scaled by a factor of 0.5 relative to the convoluted ones. The darkly shaded areas correspond to the dominant contributions to the cross-section ($\ell = 4, J = 4$ and $\ell = 4, J = 5$ for para and ortho respectively), whilst the lightly shaded areas include all initial ℓ and J contributions. The shown cross-sections were obtained using the unmorphed FCI potential.

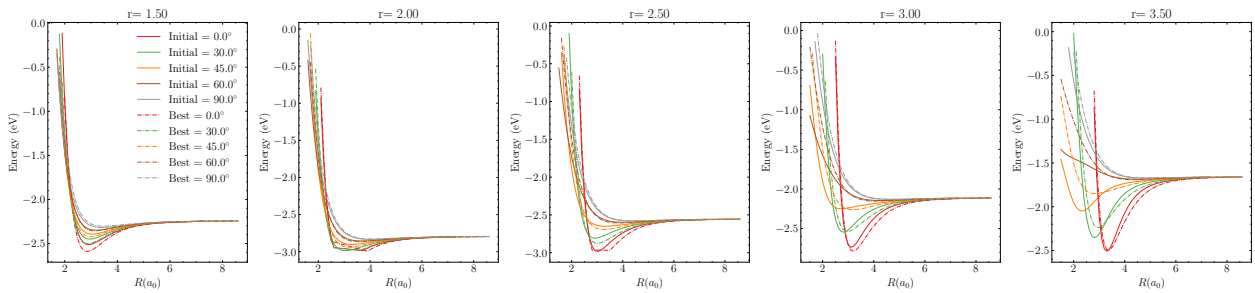


Figure S23: 1D cuts of the MRCI PES obtained from the M1 procedure along R for fixed r_{HH} and different angles (θ).

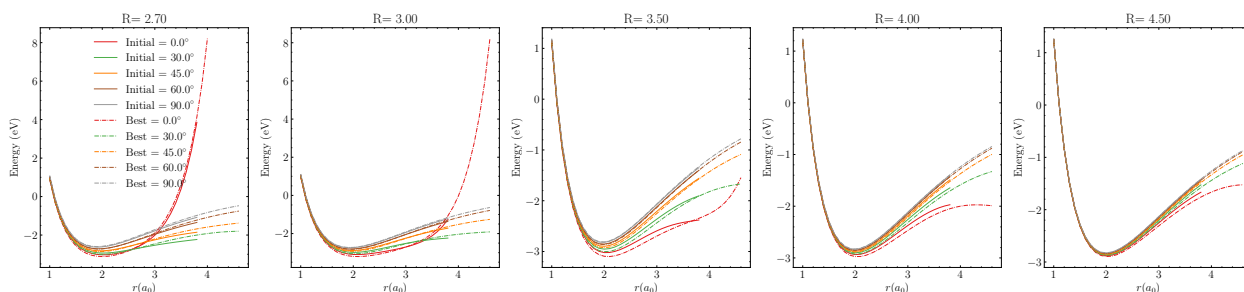


Figure S24: 1D cuts of the MRCI PES obtained from the M1 procedure along r_{HH} for fixed R and different angles (θ).

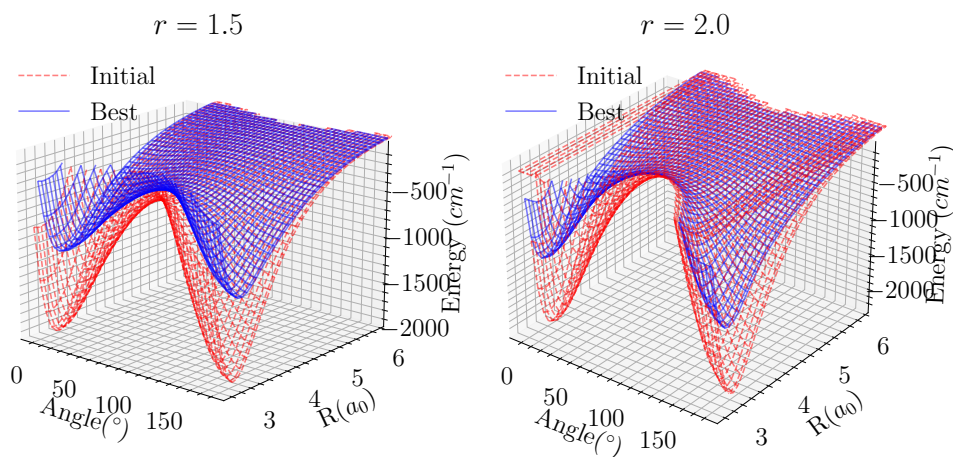


Figure S25: MP2 Potential energy surface from M1 procedure in 3D representation for fixed values of r_{HH} , on the top of the figure is indicated the value of r_{HH} . As zero of energy, it was considered the value at the given r_{HH} and $R = \infty$. Energies are in cm^{-1} and separated by 100 cm^{-1} .

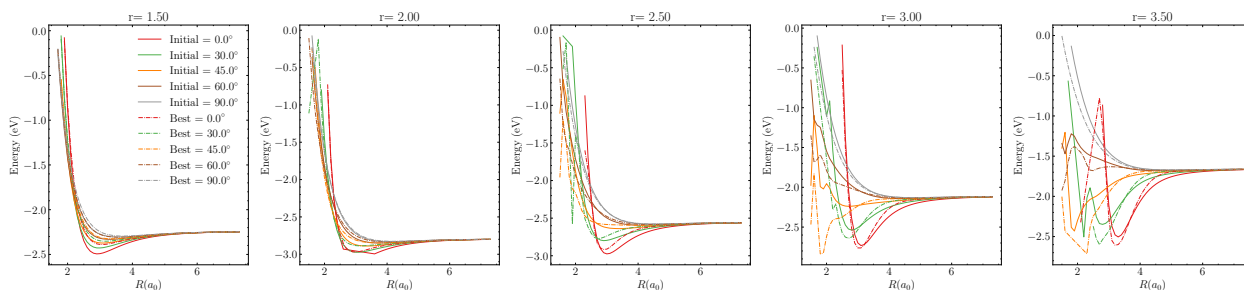


Figure S26: 1D cuts of the MP2 PES obtained from the M1 procedure along R for fixed r_{HH} and different angles (θ).

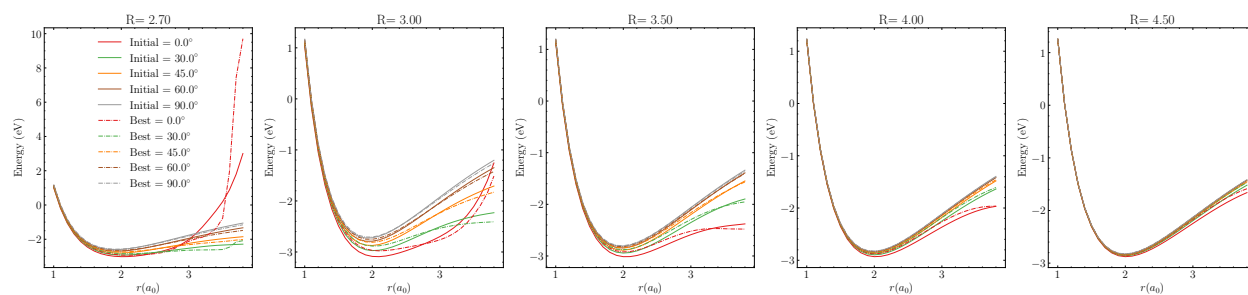


Figure S27: 1D cuts of the MP2 PES obtained from the M1 procedure along r_{HH} for fixed R and different angles (θ).

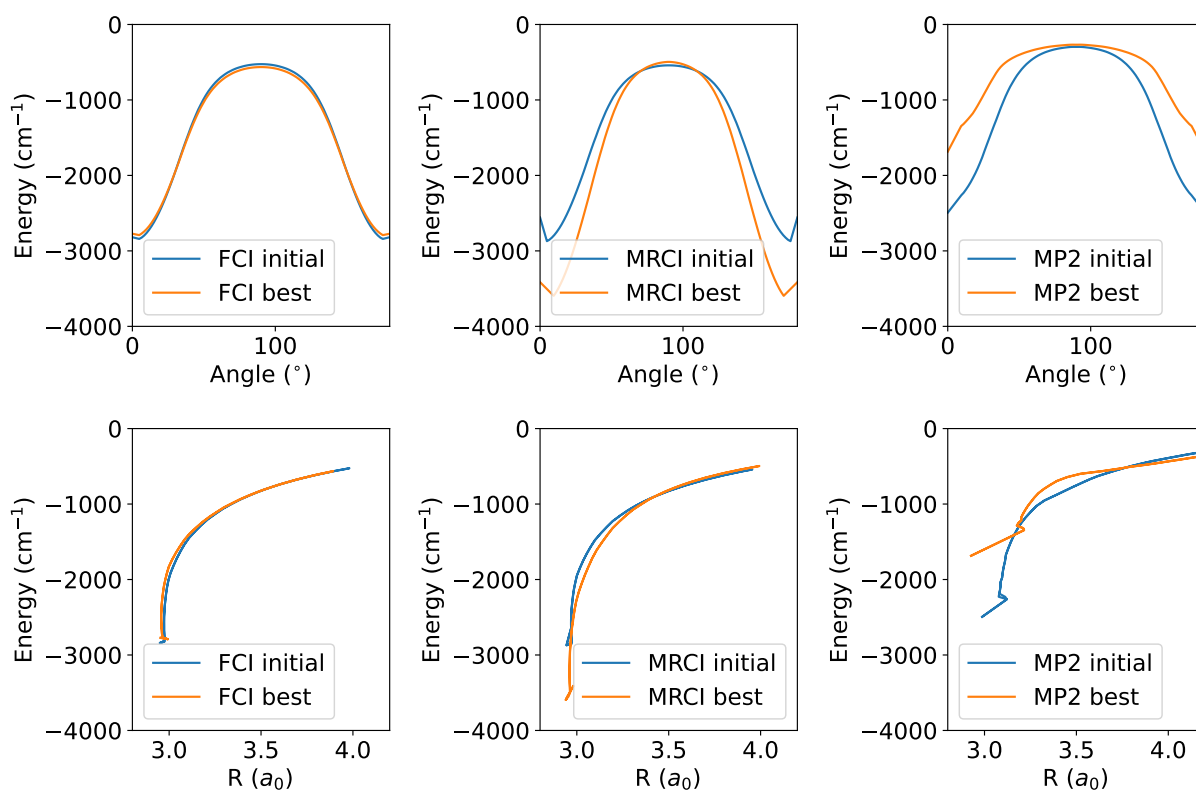


Figure S28: Minimum energy paths (MEPs) for the different surfaces obtained from the M1 method with respect to the variables θ and R . The zero of energy of the path is the energy of the separated monomers.

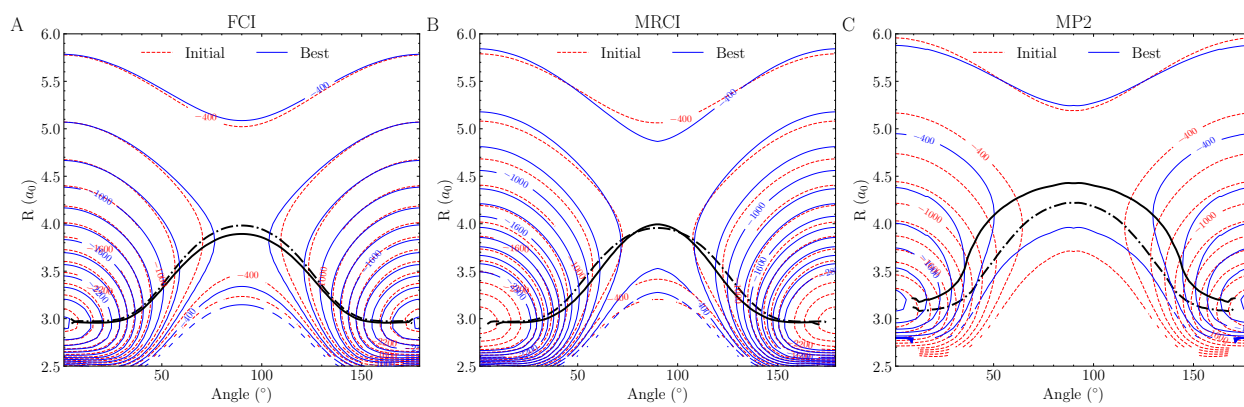


Figure S29: Minimum energy paths (MEPs) for the different surfaces studied before and after applying the morphing M1 method. In solid black, it is shown the MEP for the morph PES. In dotted black, the MEP is shown for the initial PES.